Materials Advances

ROYAL SOCIETY OF CHEMISTRY

PAPER

View Article Online
View Journal | View Issue

Check for updates

Cite this: Mater. Adv., 2024, 5, 9756

Structural, thermal, and optical spectroscopic studies of Sm^{3+}-doped $Ba_2ZnSi_2O_7$ phosphors for optical thermometry applications

Tejas,[a] A. Princy,[b] S. Masilla Moses Kennedy,[b] Vikash Mishra,[a] M. I. Sayyed,[cd] Taha A. Hanafy[e] and Sudha D. Kamath *[a]

Samarium-doped $Ba_2ZnSi_2O_7$ orange red-emitting phosphors for novel applications in temperature measurement were prepared by a solid-state synthesis method. A $Ba_2ZnSi_2O_7$ akermanite-structured Sm^{3+} phosphor was allocated to the *C*2/*c* space group and monoclinic system. Using FTIR, identification of different bonds with their vibrational modes has been done. Stimulated at 403 nm, the as-prepared phosphors show yellow (560 nm), orange (600 and 645 nm), and red (705 nm) emissions, which were also used to maximize the dopant concentration. Sm^{3+} ions may be uniformly dispersed throughout the $Ba_2ZnSi_2O_7$ matrix, and Sm^{3+} consists of irregular microparticles. Optical energy bandgap values for $Ba_2ZnSi_2O_7$ and 0.4 mol%Sm^{3+} (∼3.33 eV and ∼3.40 eV) reveal the formation of faulty energy levels in the band gap. Sm^{3+} quenching at an appropriate concentration of 0.4 mol%, with a critical distance of approximately 44.33 Å, and a θ value of 3.93, almost equal to 4, was found to be indicative of the dipole–dipole type of electric multipolar interaction. Excellent thermal stability of the PL peaks was observed in $Ba_2ZnSi_2O_7$:0.4%Sm^{3+}. A novel dual-model thermometry approach based on an adjusted Boltzmann population distribution and an exponential function would be put forward. The $Ba_2ZnSi_2O_7$:Sm^{3+} phosphor exhibited relative sensitivities of 2.02% K^{-1} based on modified Boltzmann population distribution through the FIR strategy and temperature-dependent lifetime was also employed to calculate relative sensitivities of 3.25% K^{-1} based on exponential function. In light of these experimental results, the produced Sm^{3+} doped $Ba_2ZnSi_2O_7$ phosphors can thus be a promising choice for UV-excitable warm lighting systems and non-contact optical thermometry measurements.

Received 14th September 2024,
Accepted 1st November 2024

DOI: 10.1039/d4ma00926f

rsc.li/materials-advances

Introduction

In this modern era of digitalization and industrialization, several environmental factors such as pressure, humidity, and temperature affect the environment.[1] Temperature is one such parameter that needs to be detected and controlled to have a healthy environment. In everyday life, and in chemistry, medicine, the military, and other sectors, temperature sensors are often utilized.[2–5] Electro-mechanical temperature sensors, thermocouple sensors, and optical temperature sensors are the three categories of temperature sensors.[6–8] The contact type of electro-mechanical temperature sensors, which measure temperature based on material expansion and contraction, has limited the range of applications. Because of their simplicity, usability, and broad measurement range, thermocouples are frequently utilized as temperature sensors. Nevertheless, thermocouples frequently experience limited sensitivity and interference from the surrounding environment. In recent times, optical temperature sensors have gained significant attention due to their advantages over traditional thermometers. These advantages include fast response times, high sensitivity, non-invasive detection, anti-electromagnetic interference, and the ability to measure the local microenvironment's temperature distribution.[9,10] Optical temperature sensing technology can be explored by manifesting different optical information such as luminescence intensity,[11] lifetime,[12] band shift, bandwidth,[13] and polarization.[14]

To obtain highly precise and good sensing optical thermometers it is necessary to have a chemically, thermally, and optically stable luminescent material that is preferential. Phosphors are one such material that intrigued researchers' interest for several applications including optical thermometry.

---

[a] Department of Physics, Manipal Institute of Technology, Manipal Academy of Higher Education, Manipal, Karnataka, India.
E-mail: sudha.kamath@manipal.edu
[b] Sri Siva Subramaniya Nadar College of Engineering, Tamil Nadu, India
[c] Department of Physics, Faculty of Science, Isra University, Amman, Jordan
[d] Renewable Energy and Environmental Technology Center, University of Tabuk, Tabuk, 47913, Saudi Arabia
[e] Department of Physics, Faculty of Science, University of Tabuk, Tabuk, Saudi Arabia

These inorganic materials consist of two distinct compositions, the host and activator. Selecting a suitable host is a key factor in having stable material at high temperatures, different chemical environments, and high pressures. Among different host systems, alkaline earth silicates have recently attracted attention from material scientists due to their outstanding properties. $A_2BSi_2O_7$ (A = Ca, Ba, Sr; B = Mg, Zn) generally has akermanite-based structures but it does not belong to the melilite groups of sorosilicate.[15] Trivalent lanthanide ions are unique and attractive due to their remarkable luminescence properties, which include sharp emission lines and high lumen equivalent.[16] Samarium exhibits visible and near-infrared fluorescence, and its energy level structure is complicated, with ground ^6H_J and ^6F_J multiplets and an excited $^4G_{5/2}$ level. Sm^{3+} ions are efficiently emitted in association with the intra-4f shell transition. As a result, Sm^{3+} ions frequently have a significant impact on how materials glow.[17,18] Until now, a lot of scholars have delved into and examined the characteristics of $A_2BSi_2O_7$ (A = Ca, Ba, Sr; B = Mg, Zn) phosphor hosts. Among the phosphors that have been reported are $Ca_2MgSi_2O_7$,[19] $Ca_2MgSi_2O_7:Eu^{3+}$,[20] $Ca_2MgSi_2O_7:Eu^{2+},Dy^{3+}$,[21] $Ca_2MgSi_2O_7:Eu^{2+}$,[22] $Sr_2MgSi_2O_7:Eu^{2+},Dy^{3+}$,[23] $Sr_2MgSi_2O_7:Tb^{3+},Eu^{3+}$,[24] $Ba_2MgSi_2O_7:Eu^{2+}/Eu^{3+}$,[25] $Ba_2MgSi_2O_7:Sm^{3+},Bi^{3+}$,[26] $Ca_2ZnSi_2O_7:Sm^{3+}$,[27] $Ca_2ZnSi_2O_7:Pr^{3+}$, A (A = Li^+, Na^+, K^+),[28] $Ca_2ZnSi_2O_7:Dy^{3+}$,[29] $Ca_2ZnSi_2O_7:Eu^{3+}/Al^{3+}$,[30] $Sr_2ZnSi_2O_7:Mn^{2+}$,[31] and $Sr_2ZnSi_2O_7:Dy^{3+}$.[32] Y. Patel *et al.* synthesized Dy^{3+} doped $Ba_2ZnSi_2O_7$ phosphors and studied their optical properties for solid-state lighting applications at room temperature, finding an optimum concentration of 0.2 mol%. The PL study also demonstrates low color purity values and CIE color coordinate positions to promote the emission of white light, with CCT values falling in the cool range. The double exponent approximation provided a good match for the afterglow decay curve and estimates of the fast and slow decay lifetimes were found.[15] S. Chandraker *et al.* found the PL optimum concentration to be 1.5 mol%. TL glow curve revealed a composite composition and a maximum intensity at 300 °C. The TL response rate rises linearly with increasing UV exposure, and the order of kinetics was first order. They found that for traps at increasing temperatures, the trap depth increases.[33] Z. Yang *et al.* studied Ce^{3+}, Tb^{3+} doped $Ba_2ZnSi_2O_7$ phosphors and their color-tuning properties for lighting applications. They found that in the co-doped samples, an effective energy transfer occurs from Ce^{3+} to Tb^{3+} through a non-radiative mechanism, leading to increased green emission from them. When exposed to UV radiation, the color of the particles can change from blue to green, resulting from an increase in Tb^{3+} concentrations from 0.00 to 0.06 with a fixed Ce^{3+} concentration of 0.02.[34] D. Shengzhi and his coworkers synthesized tricolour emitting triply doped $Ba_2ZnSi_2O_7:Ce^{3+},Eu^{3+},Eu^{2+}$ phosphors using a solid-state reaction method and studied their energy transfer techniques. They concluded that under UV excitation, energy would pass from $Eu^{2+} \rightarrow Eu^{3+}$ *via* Ce^{3+} upon excitation by near-UV light. As a consequence, the concentration of Eu^{3+} and Ce^{3+} could be adjusted to modify the relative strength of red, green, and blue emissions.[35] Notably, studies on Sm^{3+} doped $Ba_2ZnSi_2O_7$ at different concentrations and its structural, optical, and thermal properties have remained unexplored in the mentioned papers.

Therefore, in the current study, $Ba_2ZnSi_2O_7:xSm^{3+}$ (x = 0.2, 0.4, 0.6, 0.8, and 1.0 mol%) were synthesized utilizing the solid-state reaction technique. Various characterization approaches were used with the profound purpose of researching and integrating the optical, thermal, structural, and morphological features. We have thoroughly analyzed the TDPL and room-temperature photoluminescence (PL) spectra. We also looked at the nonradiative cross-relaxation mechanism, energy transfer, thermal stability, and temperature-dependent photoluminescence properties of the phosphor for non-contact optical thermometry applications.

Experimental details

Synthesis process

The solid-state reaction method was used to synthesize a $Ba_{(2-x)}ZnSi_2O_7:xSm^{3+}$ (x = 0.2, 0.4, 0.6, 0.8 and 1 mol%) series. $BaCO_3$ (MolyChem, 99%), ZnO (Alfa-Aesar, 99%), SiO_2 (Sigma-Aldrich, 99%), and Sm_2O_3 (MolyChem, 99.9%) were used as raw materials. Appropriate amounts of raw materials were weighed on an electronic balance, transferred to a mortar and pestle and finely ground for 1 hour with a few drops of ethanol to attain homogeneity. After grinding for 1 hour, the mixture was transferred to an alumina crucible which was kept in a muffle furnace for heating at 1200 °C for 6 hours at a heating rate of 5 °C min^{-1} in an oxygen environment. Later the sample was naturally cooled to room temperature, further ground and subjected to different characterization studies. Balanced chemical equations which were used to attain stoichiometry are given below.

$$2Ba_{2(1-x)}CO_3 + 2ZnO + 4SiO_2 + xSm_2O_3 \rightarrow 2Ba_{2(1-x)}ZnSi_2O_7{:}xSm^{3+} + 4CO_2 + \left(\frac{3}{2}\right)xO_2$$

Characterization techniques

The examination of the crystal structure of the prepared specimen was conducted through X-ray diffraction (XRD) utilizing nickel-filtered Cu-Kα radiation (λ = 1.540 Å) within the 2θ range spanning from 20° to 80°. Data collection was carried out employing a Rigaku Mini Flex 600, 5th Gen X-ray diffractometer. The determination of the lattice parameters was accomplished utilizing the FullProf suite software. An analysis of the morphology and elemental composition of the sample was performed using scanning electron microscopy (SEM) coupled with energy-dispersive X-ray spectroscopy (EDS) on a ZEISS EVO MA18 SEM equipped with an Oxford X-act detector. The investigation of the optical properties of the material was undertaken through diffuse reflectance spectroscopy (DRS) utilizing a PerkinElmer Lambda 950 spectrometer. To identify the functional groups and chemical bonds present in the sample, Fourier Transform Infrared (FTIR) spectroscopy was conducted employing a Shimadzu spectrometer. Photoluminescence excitation (PLE) and emission (PL) spectra were acquired through the utilization of a Jasco FP-8500 spectrofluorometer employing a xenon flash lamp for excitation purposes. Analysis of thermal characteristics was carried out utilizing a PerkinElmer TGA

4000 thermogravimetric analyzer (TGA) to examine the thermal stability and decomposition patterns of the specimen. Investigation into the temperature-dependent optical properties of the material was performed by measuring temperature-dependent photoluminescence spectra using an Agilent Cary Eclipse fluorescence spectrophotometer integrated with a heating unit.

Results and discussion

XRD analysis

The XRD patterns of the synthesized $Ba_{2-x}ZnSi_2O_7{:}xSm^{3+}$ (x = 0.2, 0.4, 0.6, 0.8, and 1.0 mol%) phosphors are displayed in Fig. 1. All diffraction peaks show that the Sm^{3+} ions were effectively doped into the $Ba_2ZnSi_2O_7$ host, similar to those of the standard JCPDS card PDF #28-0846.[36]

The XRD patterns of the synthesized phosphors show good agreement with the reference pattern, confirming the formation of the desired phase. However, a small shift in the XRD peaks towards higher angles is observed upon doping Sm^{3+} ions into the Ba^{2+} sites of the host lattice. This shift can be attributed to the difference in ionic radii between Sm^{3+} (1.07 Å) and Ba^{2+} (1.35 Å), which causes lattice distortion and a slight contraction of the unit cell. In order to fathom the slight shift in the XRD pattern we calculate allowed radius percentage (D_R) values, by which we can attribute the possible substitution of dopants in the host sites. The permissible relative error in the dopant radius for a successful substitution is predetermined, and the D_R number represents this limit. If the calculated D_R value falls below the threshold, typically set at 30%, the dopant ion will replace the host ion.[37] Radius difference percentage D_R can be calculated using the formula[38]

$$D_R = \left|\frac{R_1(\mathrm{CN}) - R_2(\mathrm{CN})}{R_1(\mathrm{CN})}\right| \times 100 \qquad (1)$$

where the dopant's ionic radius is R_2, and the host cation's ionic radius is R_1. The coordination number for an ion is CN. We have calculated D_R values for various combinations by using the atomic radii of the dopant and host ions. Table 1 displays the outcomes of these calculations.

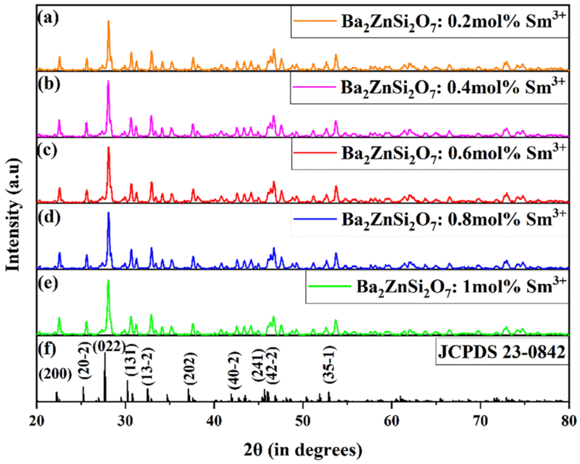

Fig. 1 (a)–(e) Powder XRD patterns of $Ba_{(2-x)}ZnSi_2O_7{:}xSm^{3+}$ (x = 0.1, 0.2, 0.4, 0.6, 0.8, 1.0 mol%) phosphors. (f) Reference pattern of $Ba_2ZnSi_2O_7$.

The data make it apparent that the D_R values for Sm^{3+} and Ba^{2+} varied from 15.67% to 49.82%. However, the values for Zn^{2+} and Sm^{3+} varied from 18.88% to 92.79%. Thus, it can be inferred that the remarkably low D_R values allow for the efficient substitution of Sm^{3+} with an atomic radius of 1.07 Å for Ba^{2+} with an atomic radius of 1.35 Å. The crystallite size was calculated using a size–strain plot using the equation given below[39]

$$(\beta_{hkl} d_{hkl} \cos\theta)^2 = \frac{\varepsilon^2}{4} + \frac{0.94\lambda}{D} {d_{hkl}}^2 \beta_{hkl} \cos\theta \qquad (2)$$

where β is the FWHM corresponding to the peak at Bragg's angle θ and d_{hkl} is the lattice distance between the (h k l) planes. The slope of the linear fit of the $(\beta_{hkl} d_{hkl} \cos\theta)^2$ *versus* $({d_{hkl}}^2 \beta_{hkl} \cos\theta)$ plot indicates the size of the crystallite. The crystallite sizes for the phosphors are found to be 20.9, 44.0, 37.5, 32.4, 35.6, and 32.9 nm respectively. The size–strain curve is shown in Fig. 2(a)–(f). The average strain was found to be 0.0084.

To comprehend the crystal structure, we perform Rietveld refinement on the $Ba_2ZnSi_2O_7{:}xSm^{3+}$ (x = 0.4 mol%) phosphor. The convergence of the refinement was seen at R_{wp} = 11.2%, R_p = 14.1%, and χ^2 = 1.68, suggesting a clear introduction of Sm^{3+} ions into the host lattice. The refined parameters are as follows: with a = 8.5013 Å, b = 10.8150 Å, and c = 8.5082 Å, we have $\alpha = \gamma = 90°$, β = 111.01°. Fig. 3 displays the Rietveld refinement of the optimum phosphor. $Ba_2ZnSi_2O_7$ is a monoclinic compound with a space group of $C2/c$ which is in line with previous reported works.[15] Fig. 4 shows the 2D structure of the Sm^{3+} doped $Ba_2ZnSi_2O_7$ phosphor in visual appearances.

FTIR studies

The molecular vibrations were identified by employing Fourier Transform Infrared (FTIR) Spectroscopy. The synthesized sample's transmittance was measured as a function of wavenumbers, and the wavenumbers that corresponded to various vibrations were determined and are listed in Table 2. Fig. 5 displays the FTIR spectra of the undoped and Sm^{3+} doped $Ba_2ZnSi_2O_7$ phosphors. The FTIR spectra provided the wavenumbers for the Ba–O stretching, Si–O asymmetric stretching, Zn–O stretching, and SiO_4 bending. Corresponding to the XRD data, the existence of identical functional groups in all the samples was confirmed and the saturated region in the spectra

Table 1 The relative error between the dopant's radius and the host ions

Host	CN	R_1	Dopant	CN	R_2	D_R
Ba^{2+}	6	1.35	Sm^{3+}	6	0.95	29.62
Ba^{2+}	6	1.35	Sm^{3+}	8	1.07	15.67
Ba^{2+}	8	1.42	Sm^{3+}	6	0.95	49.82
Ba^{2+}	8	1.42	Sm^{3+}	8	1.07	24.64
Zn^{2+}	6	0.74	Sm^{3+}	6	0.95	28.37
Zn^{2+}	6	0.74	Sm^{3+}	8	1.07	92.79
Zn^{2+}	8	0.9	Sm^{3+}	6	0.95	20.83
Zn^{2+}	8	0.9	Sm^{3+}	8	1.07	18.88
Si^{4+}	6	0.4	Sm^{3+}	6	0.95	137.5
Si^{4+}	6	0.4	Sm^{3+}	8	1.07	256.66

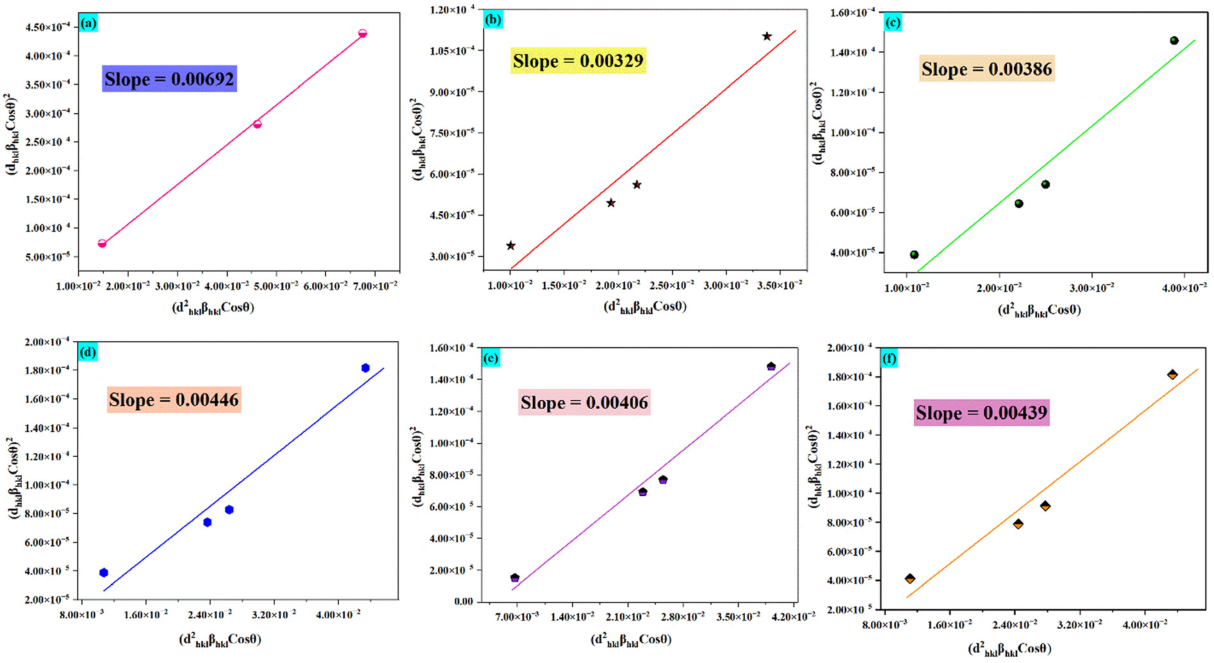

Fig. 2 (a)–(f) Size–strain plot for the prepared phosphors for crystallite size determination.

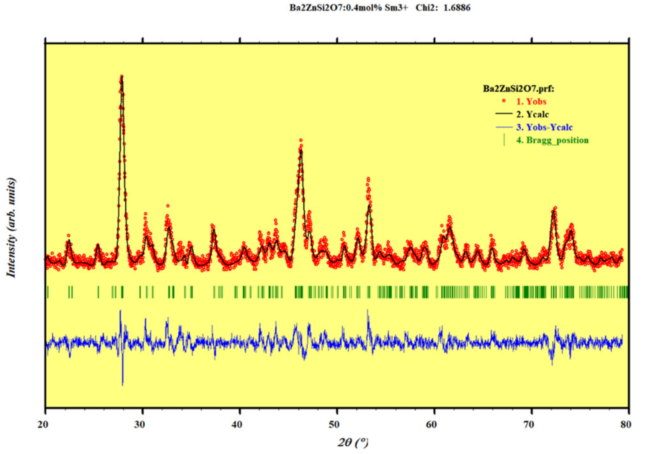

Fig. 3 Rietveld refinement plot of $Ba_{2-x}ZnSi_2O_7$:xSm^{3+} (x = 0.4 mol%) phosphors.

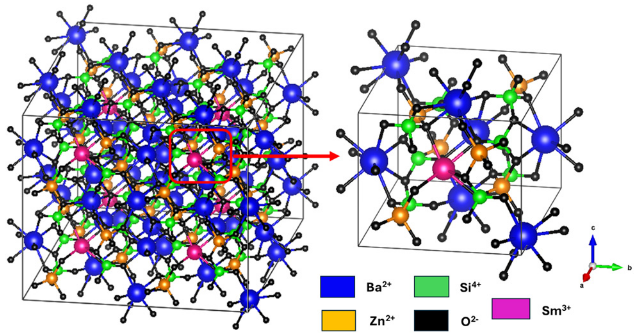

Fig. 4 Pictorial representation of Sm^{3+} doped $Ba_2ZnSi_2O_7$ phosphor.

Table 2 Different vibrational modes of the Sm^{3+} doped $Ba_2ZnSi_2O_7$ phosphor

Wavenumber (cm^{-1})	Vibrational modes
450	Ba–O stretching[40]
510	Si–O vibrations[41]
547	Si–O–Si bending[41]
633	Ba–O vibrations[40]
822	Zn–O stretching[42]
1437	Si–O vibrations[41]
1600	Si–O–Si bond stretching[41]
1795	Si–Si stretching[41]

around 800–1030 cm^{-1} was found in both the pristine and doped samples even after repeated trials.

Photoluminescence studies

We thereafter conduct photoluminescence investigations to optimize the concentration of Sm^{3+} in the derived $Ba_2ZnSi_2O_7$ matrix and investigate its optical characteristics. Fixing the emission wavelength at 600 nm, Fig. 6 shows the photoluminescence excitation spectrum of 0.4 mol% of Sm^{3+} doped Ba_2ZnSi_2O phosphor at normal temperature.

In the spectra, we observe 7 excitation peaks at 344 nm, 360 nm, 374 nm, 403 nm, 424 nm, 460 nm, and 475 nm corresponding to the transition from the ground energy level $^6H_{5/2}$ to $^4H_{9/2}$, $^4D_{3/2}$, $^6P_{7/2}$, $^4P_{3/2}$, $^6P_{5/2}$, $^4I_{13/2}$, and $^6I_{11/2}$, respectively.[43,44] Out of all the peaks that could be identified, the excitation peak with the highest intensity was found at 403 nm. It originated from the Sm^{3+} ion's transition from $^6H_{5/2}$ to $^4P_{3/2}$. As a result, to get the emission spectra of each

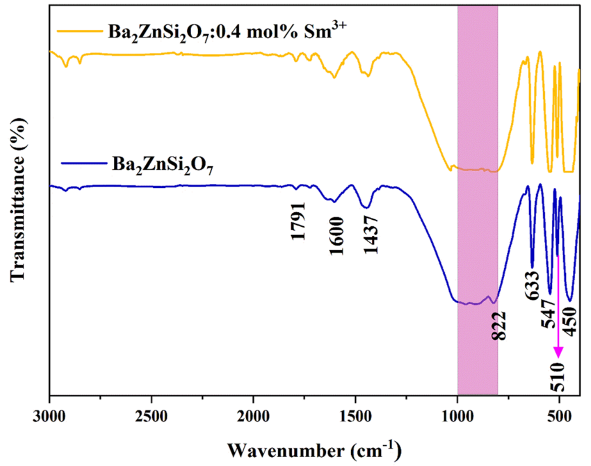

Fig. 5 FTIR spectrum of $Ba_{2-x}ZnSi_2O_7$:xSm^{3+}(x = 0, 0.4 mol%) phosphors.

synthesized phosphor, we selected 403 nm as the excitation wavelength. Fig. 7(a) manifests the emission spectra of the 0.4 mol% Sm^{3+} doped $Ba_2ZnSi_2O_7$ phosphor when excited at 403 nm. The emission spectra comprise four different peaks centered at 560, 600, 645, and 705 nm corresponding to the transitions $^4G_{5/2}$ → $^6H_{5/2}$, $^4G_{5/2}$ → $^6H_{7/2}$, $^4G_{5/2}$ → $^6H_{9/2}$, and $^4G_{5/2}$ → $^6H_{11/2}$ respectively.[45] The emission intensity that is the strongest is attributed to the $^4G_{5/2}$ → $^6H_{7/2}$ transition, which is located at 600 nm and meets the $\Delta J = \pm1$ selection criteria. It is established that the electric dipole transitions only follow the selection rule of $\Delta J \leq 6$ when J or $J' = 0$ and $\Delta J = 2, 4, 6$ otherwise, the magnetic dipole transitions follow the selection rule of $\Delta J = 0$ and ±1.[46,47] Transition $^4G_{5/2}$ → $^6H5/2$ is an allowed transition for a magnetic dipole (MD), transition $^4G_{5/2}$ → $^6H_{7/2}$ is a partially forced and partially magnetic electric–dipole (ED) transition, and transition $^4G_{5/2}$ → $^6H_{9/2}$ is a pure ED transition that is allowed and sensitive to the crystal field.[48] The degree of asymmetry increases with the strength of the ED transition. The symmetry of the local environment of the trivalent 4f ions has often been measured using the intensity ratio of ED to MD transitions.[49] The current study found that the Sm^{3+} ion exhibited a stronger $^4G_{5/2}$ → $^6H_{5/2}$ MD transition than the $^4G_{5/2}$ → $^6H_{9/2}$ ED transition, suggesting that the Sm^{3+} ions were more symmetric in the host matrix. We are aware that greater distortion from the inversion symmetry results from higher intensity ratio values. However, the obtained values were found to be within the range of 1.1–1.4 as shown in Fig. 7(b), indicating that $Ba_2ZnSi_2O_7$ exhibits no change from its original symmetry.[50]

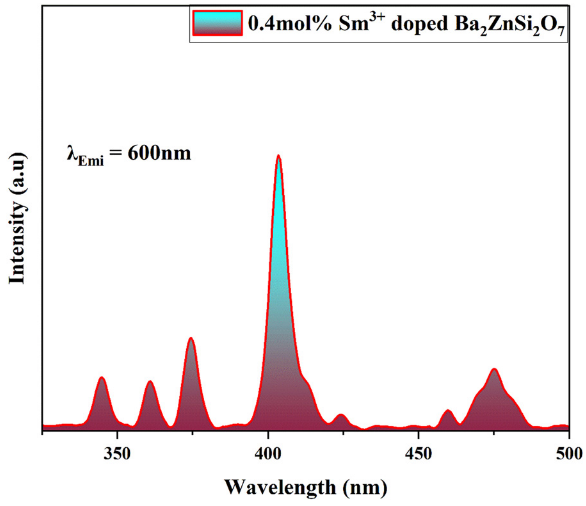

Fig. 6 PL excitation spectra of 0.4 mol% Sm^{3+} doped $Ba_2ZnSi_2O_7$ phosphor at 600 nm emission wavelength.

The transition in the emission spectra corresponding to $^4G_{5/2}$ → $^6H_{9/2}$, centered at 600 nm, has the highest intensity and is hence the main cause of the phosphor's reddish-orange emission. Furthermore, it is evident that the emission intensity achieves its peak at a Sm^{3+} concentration of 0.4 mol%. After 0.4 mol% of Sm^{3+}, the emission intensity decreases due to concentration quenching. Therefore, 0.4 mol% is considered to be the optimum Sm^{3+} concentration for the $Ba_2ZnSi_2O_7$ host. The concentration quenching can be explained using the energy transfer process arising from the cross-relaxation (CR) between Sm^{3+} ion pairs and the energy level diagram of Sm^{3+} ions as indicated in Fig. 8(a) and (b). Four energy transfer (ET) routes are available for a potential CR between two Sm^{3+} ions in $Ba_2ZnSi_2O_7$: CR1, CR2, CR3, and CR4.[51,52] These channels comprise two associated transitions with close proximate energies, as depicted in Fig. 8(b). These channels are given by

$$\text{CR1: } {}^4G_{5/2} \rightarrow {}^6F_{5/2} \approx {}^6H_{5/2} \rightarrow {}^6F_{11/2}$$

$$\text{CR2: } {}^4G_{5/2} \rightarrow {}^6F_{7/2} \approx {}^6H_{5/2} \rightarrow {}^6F_{9/2}$$

$$\text{CR3: } {}^4G_{5/2} \rightarrow {}^6F_{9/2} \approx {}^6H_{5/2} \rightarrow {}^6F_{7/2}$$

$$\text{CR4: } {}^4G_{5/2} \rightarrow {}^6F_{11/2} \approx {}^6H_{5/2} \rightarrow {}^6F_{5/2}$$

One of the two main causes of nonradiative energy transfer is exchange interaction or multipole–multipole interaction. We calculate the critical distance (R_c) in order to determine which is more dominating. Critical distance indicates the distance at which the chances of radiation emission and energy transfer are equal. In the event where nonradiative energy transfer occurred between two distinct atoms, the essential distance was determined using,[53]

$$R_C{}^6 = 0.63 \times 10^{28}\frac{Q_A}{E^4}\int f_s(E)F_A(E)\mathrm{d}E \tag{3}$$

where Q_A is the absorption cross-section, $f_s(E)$ and $F_A(E)$ represent the normalized shape of the emission band of the sensitizer and the absorption band of the activator, respectively. Nonradiative ET takes place between comparable atoms and is one of the specific examples of exchange interaction. At this time, it is possible to determine the critical distance due to exchange interaction using the equation given below,[54]

$$R_c = 2\left[\frac{3V}{4\pi x_c N}\right]^{1/3} \tag{4}$$

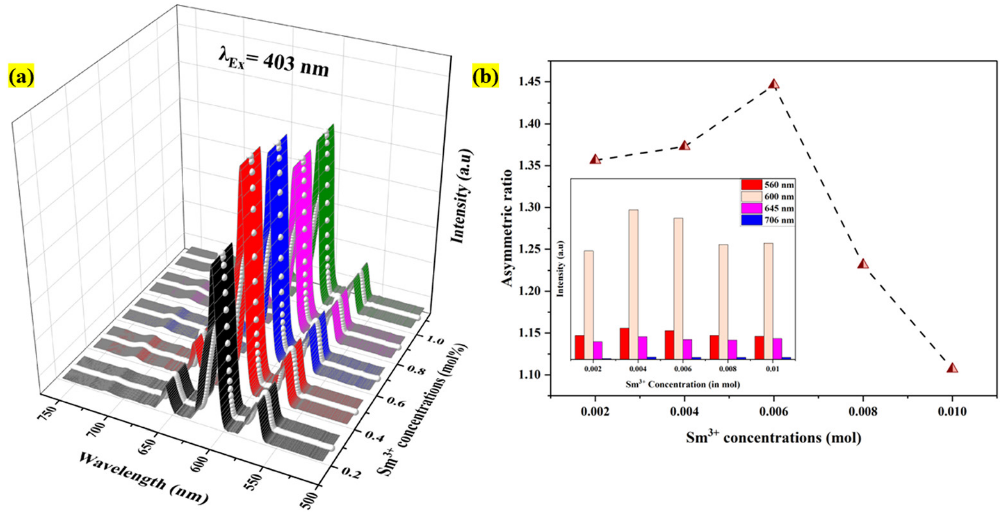

Fig. 7 (a) PL emission spectra and (b) asymmetric ratio variation with Sm^{3+} concentration, with an inset displaying the peak intensities variation for $Ba_2ZnSi_2O_7$:$x$$Sm^{3+}$ (x = 0.2, 0.4, 0.6, 0.8 and 1 mol%) phosphors.

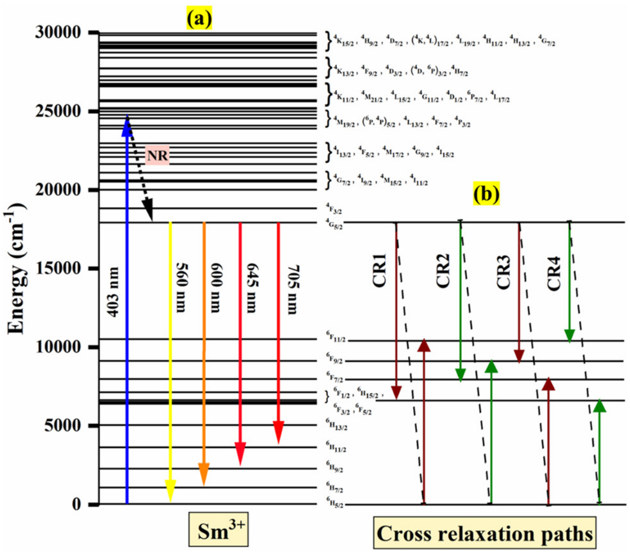

Fig. 8 (a) Energy level diagram of Sm^{3+} ions. (b) Cross relaxation paths.

where V is the volume of the unit cell, N is the number of cations per unit cell, and x_c is the ideal concentration of activator ions. Following analysis of the refining data, the findings were made as $N = 4$, $x_c = 0.004$, and $V = 730.225$ Å^3. For the present system, the predicted critical energy transfer distance is 44.33 Å.

Since R_c is a distance greater than 5 Å, the multipole–multipole interaction was primarily responsible for the energy transfer. As before, dipole–dipole (d–d), dipole–quadrupole (d–q), and quadrupole–quadrupole (q–q) interactions are subcategories of multipole–multipole interactions. Using Dexter's plot, the type of multipolar interaction may be ascertained. Dexter's hypothesis is given by,[55]

$$\log\left(\frac{I}{x}\right) = -\frac{Q}{3}\log x + A \tag{5}$$

where A is the constant and Q is the type of interaction that takes place between the rare earth ions. The electric dipole–dipole (d–d), dipole–quadrupole (d–q), and quadrupole–quadrupole (q–q) interactions, respectively, are the source of the interactions if Q = 6, 8, and 10.[56]

The Dexter plot for the phosphor with a slope of 1.31 is seen in Fig. 9(a). As a result, it was shown that $\theta = 3.93$. Given that θ was near 4, it was possible to deduce that a dipole–dipole interaction was responsible for the nonradiative energy transfer from one excited ion to another ion. Another thing to keep in mind is that when the dopant ion Sm^{3+} is substituted for Ba^{2+} in the host lattice, an imbalance in charges occurs, leading to a net positive charge at the point of substitution. Ba^{2+} will cause defects (vacancies) in the charge balance, distorting the host lattice. These flaws lower the photoluminescence intensity by producing electron-capturing centers. Therefore, for the host lattice,[55]

$$2[\mathrm{SmO}_{12}]^{\bullet\bullet}+\left[\mathrm{V}_{\mathrm{Ba}}^{\prime\prime}\mathrm{O}_{12}\right]_{\mathrm{Complex}}\rightarrow 2[\mathrm{SmO}_{12}]^{\times}+\left[\mathrm{V}_{\mathrm{Ba}}^{\times}\mathrm{O}_{12}\right]_{\mathrm{Complex}} \tag{6}$$

where $[\mathrm{SmO}_{12}]^{\bullet\bullet}$ is the donor, $\left[\mathrm{V}_{\mathrm{Ba}}^{\prime\prime}\mathrm{O}_{12}\right]_{\mathrm{Complex}}$ is the acceptor.

$$\left[\mathrm{V}_{\mathrm{Ba}}^{\times}\mathrm{O}_{12}\right]_{\mathrm{complex}}+\grave{e}_{\mathrm{excited}}\rightarrow\left[\mathrm{V}_{\mathrm{Ba}}^{\prime}\mathrm{O}_{12}\right]_{\mathrm{complex}} \tag{7}$$

$$\left[\mathrm{V}_{\mathrm{Ba}}^{\prime}\mathrm{O}_{12}\right]_{\mathrm{complex}}+\grave{e}_{\mathrm{excited}}\rightarrow\left[\mathrm{V}_{\mathrm{Ba}}^{\prime\prime}\mathrm{O}_{12}\right]_{\mathrm{complex}} \tag{8}$$

The lattice charge's neutrality before excitation by 403 nm is represented by eqn (6). Eqn (7) and (8) relate to electron self-trapping following excitation by 403 nm radiation. Eqn (1) indicates that in the sample $Ba_2ZnSi_2O_7$:0.4 mol% Sm^{3+}, the barium vacancy is created, and two samarium atoms replace one barium atom. Hence, the two-fold barium vacancy created in the sample of $Ba_2ZnSi_2O_7$:0.4 mol% Sm^{3+}, compared to $Ba_2ZnSi_2O_7$:0.2 mol% Sm^{3+}, results in the double self-trapping. Consequently, the energy transfer mechanism involving cross-relaxation

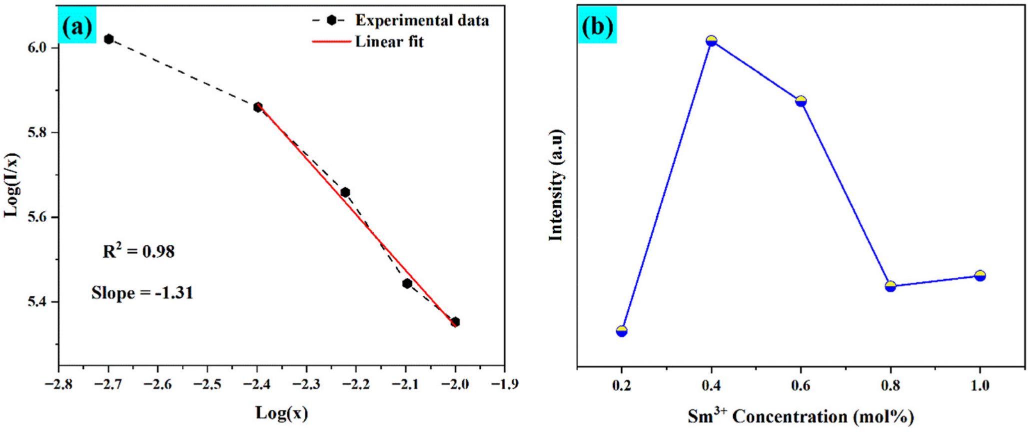

Fig. 9 (a) Dexter plot for the phosphors that were produced and (b) illustrates the concentration of Sm^{3+} alters emission intensity.

between the neighbouring Sm^{3+} ions and energy transfer between Sm^{3+} ions and barium vacancies causes a considerable decrease in photoluminescence intensity.[57,58] As seen in Fig. 10, A further explanation for emission intensity is the energy transfer between Sm^{3+} and Ba^{2+} vacancies.

The most common approach for characterizing and expressing color that is produced by phosphor material is the Commission Internationale de I'Eclairage (CIE) system. Fig. 11 displays the CIE chromatic diagram of synthesized $Ba_{2-x}ZnSi_2O_7$:$x$$Sm^{3+}$ (x = 0.2, 0.4, 0.6, 0.8, and 1.0 mol%) phosphor at excitation wavelength at 403 nm, which is derived from emission spectra. These CIE coordinates were calculated using these equations,[59]

$$x = \frac{X}{X+Y+Z} \tag{9}$$

$$y = \frac{Y}{X+Y+Z} \tag{10}$$

Using these CIE coordinates we have calculated Colour-correlated temperature (CCT) values by approximating McCamy's equation,[60,61]

$$\mathrm{CCT} = -449n^3 + 352n^2 - 6823.3n + 5520.33 \tag{11}$$

where n represents the inverse slope line and is computed as $n = \dfrac{(x_\mathrm{p}-x_0)}{(y_\mathrm{p}-y_0)}$ where the chromatic coordinates of the prepared phosphor are represented by (x_p, y_p) and the epicenter of convergence is represented by (x_0, y_0) = (0.332, 0.186). To compute λ_d, a line connecting (x_p, y_p) and (x_0, y_0) will be drawn. It is then extended to a point on the edge of the diagram after that. The wavelength that matches the coordinates of the perimeter is called λ_d. With the use of all these findings, we can use the formula to determine color purity.[62]

$$\mathrm{C.P.} = \frac{\sqrt{(x_\mathrm{p}-x_0)^2+(y_\mathrm{p}-y_0)^2}}{\sqrt{(x_\mathrm{d}-x_0)^2+(y_\mathrm{d}-y_0)^2}} \times 100 \tag{12}$$

Table 3 presents the CCT, λ_d, and C.P. values for the Sm^{3+} doped $Ba_2ZnSi_2O_7$ phosphors. The phosphor is seen to have a C.P. of about 100% and CCT values that are in the range of 1416–1491 K, suggesting that it might be a good option for the production of warm light.[63]

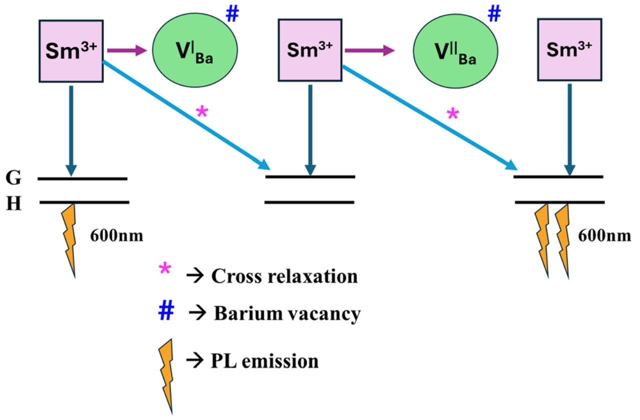

Fig. 10 Energy transfer mechanism Sm^{3+} to Ba^{2+} vacancy.

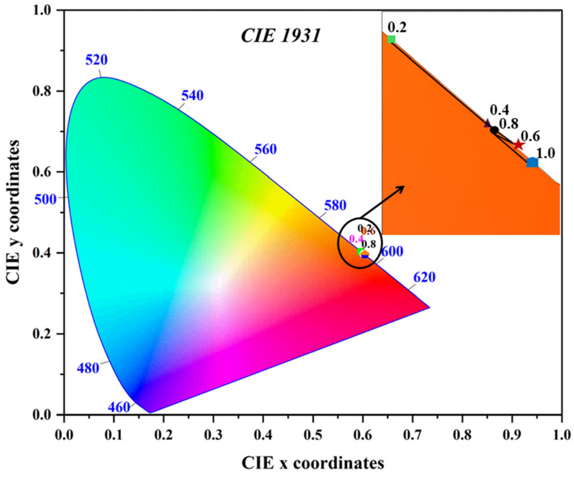

Fig. 11 CIE chromaticity coordinates of $Ba_{2-x}ZnSi_2O_7$:$x$$Sm^{3+}$ (x = 0.2, 0.4, 0.6, 0.8 and 1.0 mol%) phosphors.

Table 3 CIE chromaticity coordinates (x_p, y_p), dominant wavelength (λ_d), color purity (C.P.), and CCT values for $Ba_{2-x}ZnSi_2O_7$:$x$$Sm^{3+}$ (x = 0.2, 0.4, 0.6, 0.8 and 1.0 mol%)

Sm^{3+} concentrations (mol%)	(x_p, y_p)	(x_d, y_d)	λ_d (nm)	C.P. (%)	CCT (K)
0.2	(0.5965, 0.4030)	(0.3592, 0.5460)	593.8	100.0	1491
0.4	(0.6017, 0.3976)	(0.3665, 0.5449)	594.8	100.0	1439
0.6	(0.6033, 0.3963)	(0.3685, 0.5447)	595.1	100.0	1426
0.8	(0.6021, 0.3973)	(0.3669, 0.5448)	594.9	100.0	1436
1.0	(0.6042, 0.3951)	(0.3699, 0.5443)	595.3	100.0	1416

Surface morphology

Next, the optimized phosphor's morphological characteristics were examined using a scanning electron microscope (SEM). Fig. 12(a)–(h) shows the elemental mapping for energy dispersive Xray (EDX) and SEM images for $Ba_{2-x}ZnSi_2O_7$:$x$$Sm^{3+}$ (x = 0.4 mol%). The even distribution of every element in a chosen region is verified by EDX. The SEM photos clearly show that the synthesized phosphor particles had uneven shapes which caused the grains to aggregate into an agglomerated structure. This characteristic is inherent in the morphology of phosphors made by the high-temperature solid-state technique.[64]

UV-vis-NIR spectra analysis

The reflection and absorbance spectra are shown in Fig. 13(A). Due to spin and parity-allowed ligand (O^{2-}) to metal charge transfer (CT) transitions by the Sm^{3+} ions in the $Ba_2ZnSi_2O_7$ host, the shorter wavelength range displays broadband. Sm^{3+} ion 4f–4f transitions are linked to the absorption peaks at around 400 nm. The spectrum demonstrates the transitions $^6H_{5/2} \rightarrow {}^6F_{9/2}$, $^6H_{5/2} \rightarrow {}^6F_{7/2}$, and $^6H_{5/2} \rightarrow {}^6F_{5/2}$ are attributed to the wide peaks at about 1078, 1218, and 1392 nm, respectively.[65,66] The band gap of the samples was calculated using Tauc's equation,[67]

$$[F(R)h\vartheta]^n = A(h\vartheta - E_g) \qquad (13)$$

where $F(R)$ is a Kubelka–Munk function, A is a proportional constant, E_g is the optical band gap value, and n = 2 for an indirect transition or $n = \frac{1}{2}$ for a direct transition,[67]

$$F(R) = \frac{\alpha}{S} = \frac{(1-R)^2}{2R} \qquad (14)$$

As seen in Fig. 13(B), the predicted E_g values for pure host matrix are about 3.33 eV and for 0.4 mol% Sm^{3+} ion doped $Ba_2ZnSi_2O_7$ were found to be 3.40 eV, respectively. On doping there is a slight increase in the energy band gap.

Moreover, we may use the Dimithrov–Sakka equation to find the material's refractive index,[68]

$$\frac{n^2-1}{n^2+2} = 1 - \sqrt{\frac{E_g}{20}} \qquad (15)$$

where n is the material's refractive index and E_g is its optical energy band gap. Refractive indices were determined to be 5.35 for undoped $Ba_2ZnSi_2O_7$ and 5.27 for $Ba_2ZnSi_2O_7$ doped with 0.4 mol% Sm^{3+}.

Understanding the kind of Sm^{3+}–ligand bond found in the produced phosphors is possible by calculating the values of the bonding parameter (δ) and nephelauxetic ratio (β). One may

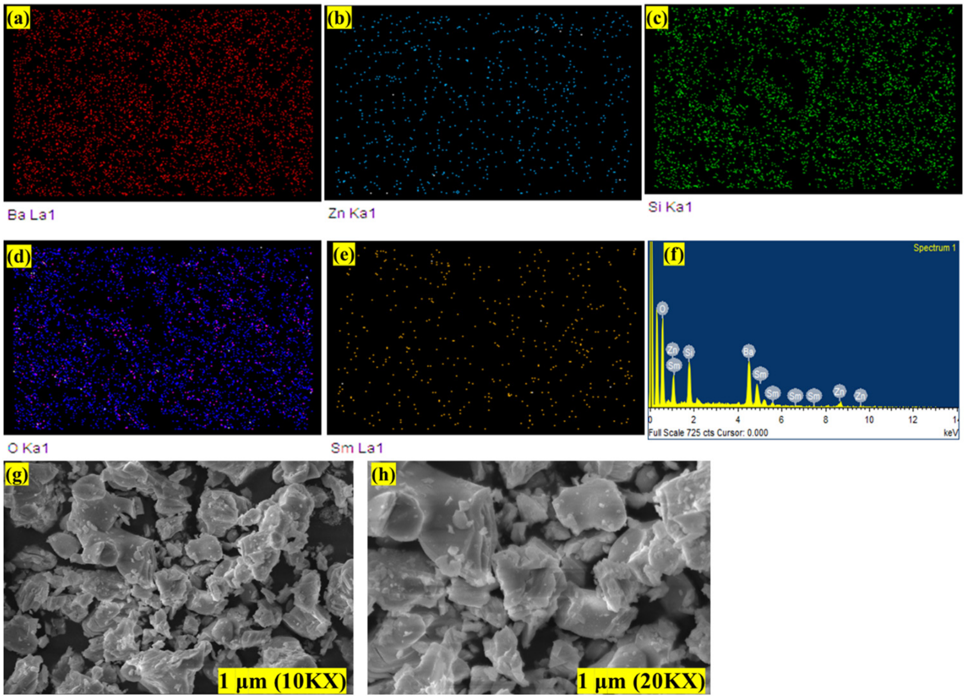

Fig. 12 (a)–(e) Elemental mapping (f) EDAX spectra (g) and (h) SEM images at different magnifications of $Ba_{2-x}ZnSi_2O_7$:$x$$Sm^{3+}$ (x = 0.4 mol%) phosphor.

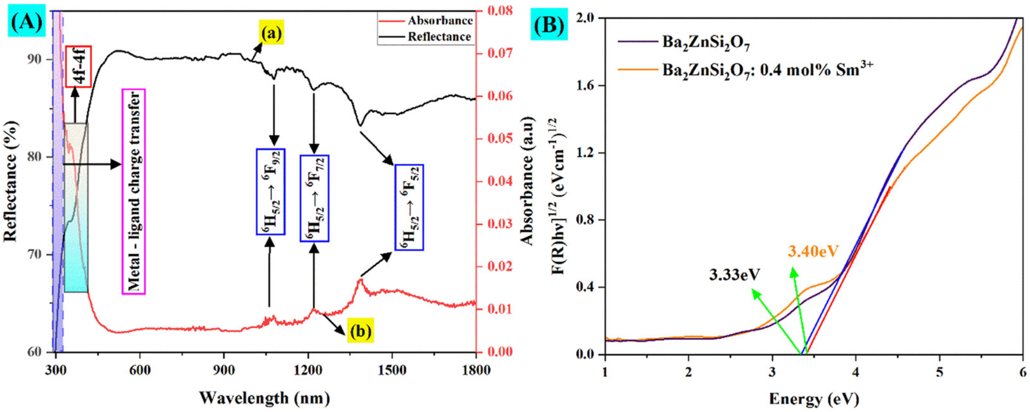

Fig. 13 (A) (a) and (b) Reflectance and absorption band spectra. (B) Tauc plot for $Ba_{2-x}ZnSi_2O_7$:xSm^{3+}(x = 0.4 mol%) phosphors.

find the nephelauxetic ratio by utilizing,[69]

$$\beta = \frac{\vartheta_c}{\vartheta_a} \quad (16)$$

where ϑ_c and ϑ_a are the wave numbers for a certain Sm^{3+} transition in the host and aqueous solution, respectively. One may use an equation to calculate the bonding parameter (δ),[69]

$$\delta = \frac{1-\bar{\beta}}{\bar{\beta}} \times 100 \quad (17)$$

where $\bar{\beta}$ is the average nephelauxetic ratio value. The specific kind of Sm^{3+}–ligand bond is classified as ionic when δ is negative and as covalent when δ is positive.[70] The band assignments, nephelauxetic ratio (β), and bonding parameter (δ) for the system are listed in Table 4. Since the bonding value was discovered to be −1.6264, $\delta < 0$. Due to the negative value of the bonding parameter, the Sm^{3+}–ligand bonds are ionic in nature.

Thermo-gravimetry analysis

The study focused on the thermal stability of an optimized $Ba_{2-x}ZnSi_2O_7$:xSm^{3+} (x = 0.4 mol%) phosphor. The produced phosphor exhibits good thermal stability at high temperatures (up to 600 °C), according to the results. Fig. 14 illustrates that not much mass loss was seen. A small amount of mass loss is emphasized in the inset figure.

Lifetime measurements studies

We determine the lifetimes of $Ba_{2-x}ZnSi_2O_7$:xSm^{3+} (0.2 mol% ≤ x ≤ 1 mol%) by measuring their decay curves at room temperature. The results are displayed in Fig. 15(a). With 403 nm excitation wavelength, and 600 nm emission wavelength the measurement has been made. All decay curves were fitted using the single – exponential function, which is given as ref. 71 and 72,

$$I(t) = I_0 + \exp\left(-\frac{t}{\tau}\right) \quad (18)$$

where I_0 and $I(t)$ are the luminescence intensities at times 0 and t, respectively, and τ is the decay time.

The decay time values of $Ba_2ZnSi_2O_7$:xSm^{3+} (x = 0.2, 0.4, 0.6, 0.8 and 1 mol%) phosphors are 2.133, 1.966, 1.962, 1.849 and 1.838 ms respectively.[73] The variation of decay time with different concentrations was shown in Fig. 15(b).

Table 4 Band transitions, nephelauxetic ratio (β), and bonding parameter δ for the 0.4 mol% Sm^{3+} phosphors in $Ba_2ZnSi_2O_7$

Sl. no.	Transitions	ϑ_c (cm^{-1})	ϑ_a (cm^{-1})	β
1	$^6H_{5/2} \rightarrow {}^6F_{9/2}$	9233	9136	1.0107
2	$^6H_{5/2} \rightarrow {}^6F_{7/2}$	8151	7977	1.0218
3	$^6H_{5/2} \rightarrow {}^6F_{5/2}$	7253	7131	1.0171
$\bar{\beta}$				1.0165

Temperature-dependent optical studies

Fig. 16(a) shows the $Ba_{2-x}ZnSi_2O_7$:xSm^{3+} (x = 0.4 mol%) phosphor with variable-temperature fluorescence spectra in the 303–483 K range. It is clearly visible that the emission of Sm^{3+} ions is evident with different temperatures. All the emission peaks that we observed at room temperature were observed at high temperatures, but the intensity counts were decreased by about 30–40% compared to room temperature. At 560, 600, 645, and 705 nm, distinct emission was seen, which corresponded to the transitions $^4G_{5/2} \rightarrow {}^6H_{5/2}$, $^4G_{5/2} \rightarrow {}^6H_{7/2}$,

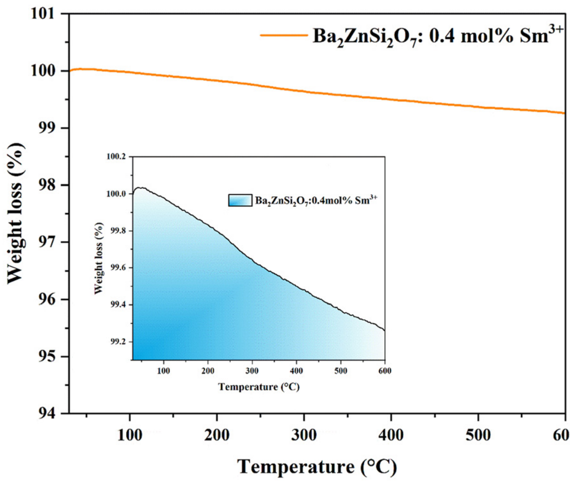

Fig. 14 $Ba_{2-x}ZnSi_2O_7$ TGA curve:xSm^{3+} (x = 0.4 mol%) phosphors, with an inset graph that displays mass loss on a magnified scale.

$^4G_{5/2} \rightarrow {}^6H_{9/2}$, and $^4G_{5/2} \rightarrow {}^6H_{11/2}$, in that order.[74,75] Fig. 16(b) clearly shows the decrease in the normalized emission intensity at elevated temperatures. Even at higher temperatures, the position of the peaks remained as such compared to room temperature.

The quenching of intensity at elevated temperature can be described using a configurational coordination model as shown in Fig. 16(c). At 403 nm excitation, the electron excites to the excited state from the ground state. Since the electrons are not stable at higher energy levels for longer periods, they eventually try to lose their energy by making a transition from higher energy to lower energy level. Here, we can get strong red emission due to the transition from higher energy to ground state followed by a large number of electrons traveling through a non-radiative transition from the lowest point of the $^4G_{5/2}$ energy level to the ground state. Due to the strong phonon–electron interaction, it is possible that the excited state electrons passed the activation energy (E_a) (Route 1) and entered the CTB directly (Route 2). When electrons follow route 3, they eventually arrive in their ground state and radiate heat. The thermal quenching temperature (T_Q) of the $Ba_2ZnSi_2O_7$:Sm^{3+} phosphor may thus be used to assess its thermal stability. The term "quenching temperature" refers to the temperature at which the photoluminescence emission emits half of its initial intensity.[76] The Boltzmann sigmoidal fit plot, which is used to calculate the thermal quenching temperature (T_Q), is shown in Fig. 16(d). The Boltzmann sigmoidal fitting function is given by ref. 77,

$$I(T) = A_2 + \frac{A_1 - A_2}{1 + e^{\frac{(T - T_Q)}{dT}}} \tag{19}$$

$I(T)$ is the normalized emission intensity at a given temperature. A_1 and A_2 represent the starting and ultimate emission intensity levels, respectively. Since we standardized the emission intensity value in this instance between 1 and 0, $A_1 = 1$, $A_2 = 0$. T_Q is the sigmoid's center, while dT displays its fluctuation.[78] From the fitted plot, the quenching temperature was found to be 367 ± 5 K, which represented it has good thermal stability.

Fig. 17 displays the FWHM variation of TDPL emission peaks with temperature for the $Ba_2ZnSi_2O_7$:Sm^{3+} ($x = 0.4$ mol%) phosphor. It is evident that the FWHM of the emission increased gradually for 562 nm, 600 nm, and 646 nm emission. A small emission peak at 706 nm decreases at first and then increases due to interactions of RE–RE ions in the host. The FWHM of the emission spectrum increases due to a strong interaction between the thermally active phonons and the thermally activated luminescent core. At high temperatures, the electron–phonon interaction becomes more noticeable due to an increase in the phonon population density.[79] Mathematically, an increase in FWHM is given by,

$$\Gamma(T) = \sqrt{8 \ln 2} \times \hbar\omega \times \sqrt{S \coth\left(\frac{\hbar\omega}{2kT}\right)} \tag{20}$$

where $\hbar\omega$ represents the effective phonon energy, $\Gamma(T)$ indicates the temperature-dependent FWHM, and k and S stand for the Boltzmann and Huang–Rhys parameters, respectively.[80] The intensity ratios of anti-Stokes peaks to Stokes peaks (I_a/I_s) followed the Boltzmann-type distribution function, which contributed to the difference in thermal behavior provided by,[81]

$$\frac{I_a}{I_s} = C \exp\left(-\frac{\hbar\omega}{kT}\right) \tag{21}$$

where T is the absolute temperature and C is the proportionality constant. One potential technique for thermal sensing is to use the variation in the intensity of the anti-Stokes emission line concerning the Stokes emission line. Eqn (21) may be taken as natural logarithmic,[82,83]

$$\ln\left(\frac{I_a}{I_s}\right) = \ln(C) - \frac{\hbar\omega}{kT} \tag{22}$$

where I_a and I_s are 562 and 600,706 nm, respectively. The fluctuation of $\log_e(I_{562}/I_{600})$ *vs.* $1/T$ and $\log_e(I_{562}/I_{706})$ are seen in Fig. 18(a) and (b) respectively. After doing a linear fit on the graph, $\log_e \frac{I_{562}}{I_{706}} = 0.94 - \frac{-94.41}{T}$ with $\hbar\omega/k = 94.41$ K was found to be the best match. It was found that the fitted value of phonon energy $\hbar\omega$ was 65.61 cm^{-1}. Similarly, for $\log_e \frac{I_{562}}{I_{600}} = -0.26 - \frac{-91.84}{T}$ with $\hbar\omega/k = 91.84$ K was discovered to be the ideal fit. It was discovered

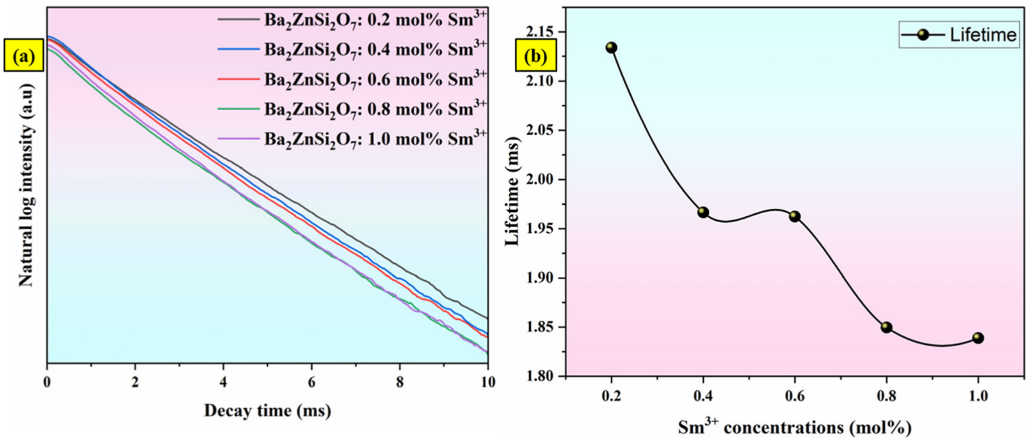

Fig. 15 (a) The decay curves (b) variation of decay time for $Ba_2ZnSi_2O_7$:xSm^{3+} (x = 0.2, 0.4, 0.6, 0.8 and 1 mol%) phosphors.

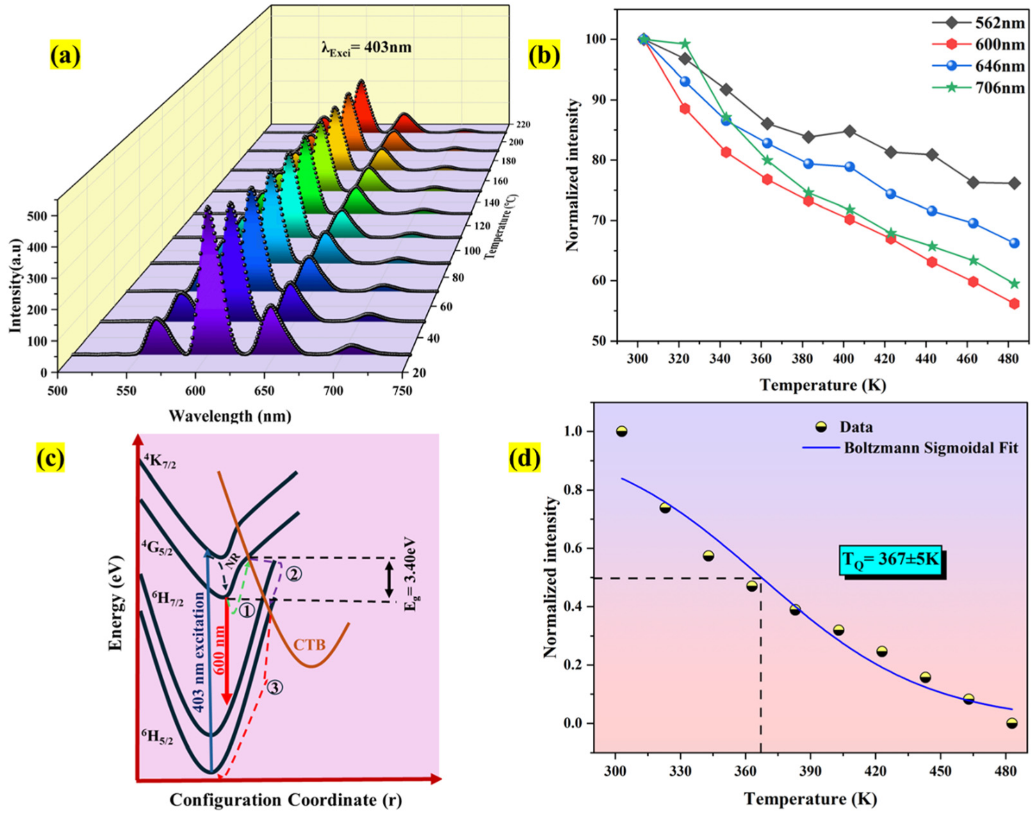

Fig. 16 (a) PL emission spectra that are temperature-dependent (b) normalized TDPL emission intensity (c) the schematic diagram for configurational coordinates (d) Boltzmann fit for the temperature-dependent emission spectra of phosphors $Ba_2ZnSi_2O_7$:Sm^{3+}.

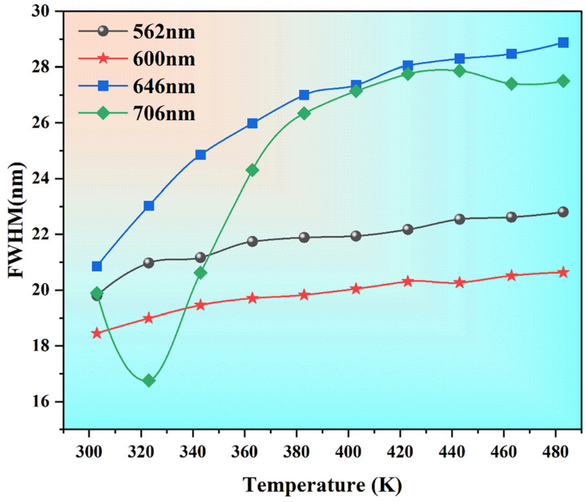

Fig. 17 Changes in FWHM of emission peaks at various temperatures for $Ba_{2-x}ZnSi_2O_7$:xSm^{3+} (x = 0.4 mol%) phosphors.

that 63.83 cm^{-1} was the fitting value of phonon energy. These findings suggested that temperature sensing may also be accomplished with the optimized phosphor due to the lowest phonon energy.

The activation energy, or ΔE, is the energy difference between the ground state and the lowest excited state. Electrons in lower excited levels will be thermally aroused to higher energy states if the phosphor receives more thermal energy than ΔE. Then, in order to get back to the ground state, they will pass *via* the crossover points between the excited and ground states.[84] The thermal stability of the phosphor will rise along with the magnitude of ΔE as non-radiative relaxation rises with temperature. One may define activation energy by applying the Arrhenius equation, which is provided by,[85]

$$I = \frac{I_0}{1 + C\exp\left(-\frac{\Delta E}{kT}\right)} \tag{23}$$

where intensities at lower and higher temperatures are denoted, respectively, by I and I_0. The symbols ΔE, k, and C represent the activation energy, Boltzmann constant, and constant, respectively. We took natural logs on both sides of eqn (23) to simplify it and get ΔE,

$$[\ln(I_0/I) - 1] = \ln C - \frac{\Delta E}{kT} \tag{24}$$

In Fig. 18(c) we have calculated the activation energy which was found to be 0.359 eV for 600 nm respectively. To more clearly see the distinction between the luminous thermal quenching trend of different emissions of Sm^{3+} as a function of temperature is displayed in Fig. 18(d).

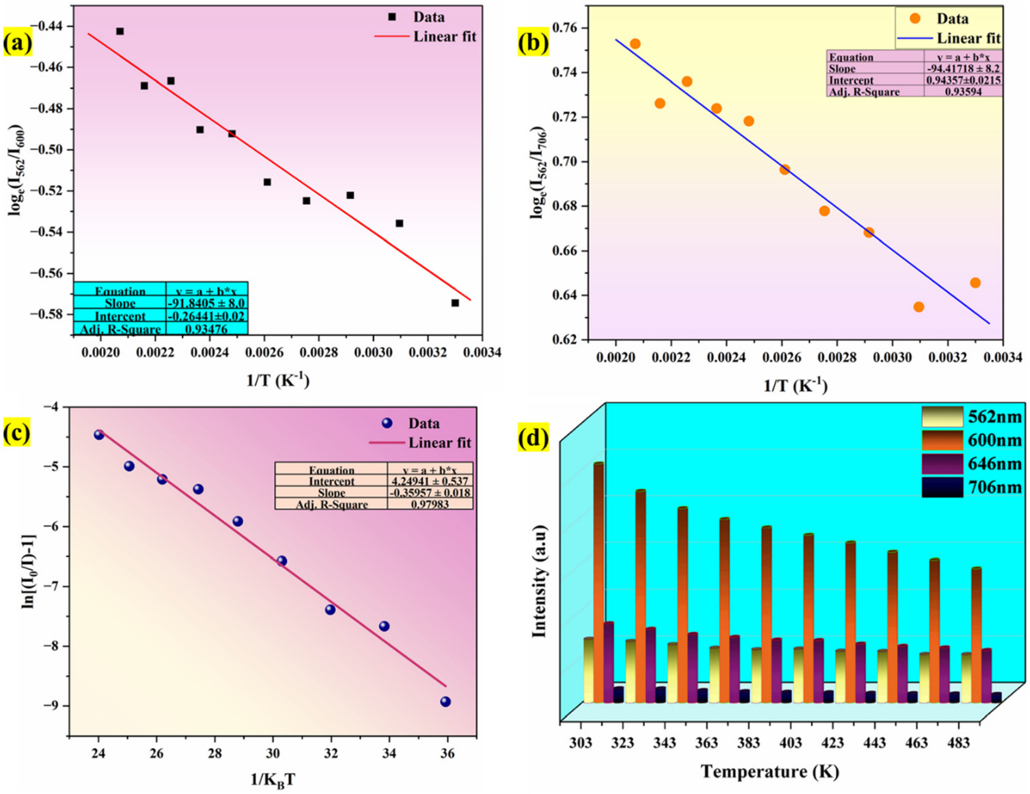

Fig. 18 (a) Plot of log(I_{562}/I_{600}) *v/s* 1/*T* (b) plot of log(I_{562}/I_{706}) *v/s* 1/*T* (c) Arrhenius plot for 600 nm emission (d) intensity variation of different emission peaks at various temperatures for $Ba_{2-x}ZnSi_2O_7{:}xSm^{3+}$ (x = 0.4 mol%) phosphors.

Thermal sensing studies

Fluorescence intensity ratio method (FIR). Exploring the temperature dependence of FIR between two different emissions of Sm^{3+} is essential to further understand the temperature sensing behavior of the $Ba_2ZnSi_2O_7{:}xSm^{3+}$ (x = 0.4 mol%) phosphor. The link between temperature and integrated PL intensity of the Sm^{3+} anti-Stokes peak (I_{as}) and Stokes peak (I_s) may be expressed using the Struck and Fonger hypothesis.[86] The relative population of the thermally related energy levels follows the Boltzmann distribution law. The Boltzmann distribution of thermally linked energy levels and temperature affects emission intensities. The following expression can be used to express the relationship between temperature and PL intensity of the excited rare earth ions,[87,88]

$$\mathrm{FIR} = \frac{I_{as}}{I_s} \approx A e^{\frac{-\Delta E}{k_B T}} + B \tag{25}$$

where k_B is the Boltzmann constant, B is an offset parameter, ΔE is the activation energy required to move an electron from its emission state to the quenching state, and A is the proportional parameter. The experimental data and the fitting outcomes derived from the above equation represent the actual points and lines, respectively. Fig. 19(a) shows the variation of FIR of (I_{600}/I_{562}) intensities concerning temperature and we can observe it is decreased at elevated temperatures from 303–483 K. Additionally, Fig. 19(b) illustrates the change in the FIR of (I_{706}/I_{562}) intensities with temperature. It also decreased monotonically with temperature. Both the plots were fitted with eqn (25) which is given by,

$$\mathrm{FIR}\left(\frac{I_{600}}{I_{562}}\right) = -478.2552 + 479.6813 \times \exp\left(\frac{1.4174}{T}\right) \tag{26}$$

$$\mathrm{FIR}\left(\frac{I_{706}}{I_{562}}\right) = 0.7960 - 0.7221 \times \exp\left(\frac{-74.7472}{T}\right) \tag{27}$$

It is crucial to look into the sensing sensitivity of $Ba_2ZnSi_2O_7{:}Sm^{3+}$ phosphor for temperature sensing to learn more about temperature sensitivity. The performance of the temperature sensors may be assessed using two important parameters: relative sensitivity (S_R) and absolute sensitivity (S_A). The S_R and S_A, which are the relative and absolute changes in the FIR in response to temperature fluctuations, may be obtained using the following equation.[89,90]

$$S_R = 100\% \times \left|\frac{1}{\mathrm{FIR}}\frac{\partial \mathrm{FIR}}{\partial T}\right| = \frac{A e^{\frac{-\Delta E}{k_B T}}}{A e^{\frac{-\Delta E}{k_B T}} + B} \times \frac{-\Delta E}{k_B T^2} \tag{28}$$

$$S_A = \frac{|\partial \mathrm{FIR}|}{|\partial T|} = A e^{\frac{-\Delta E}{k_B T}} \times \frac{-\Delta E}{k_B T^2} \tag{29}$$

The values of absolute and relative sensitivity at different temperatures for (I_{600}/I_{562}) and (I_{706}/I_{562}) are measured and shown in Fig. 19(c) and (d) respectively. The absolute and relative sensitivity decreased monotonically for higher

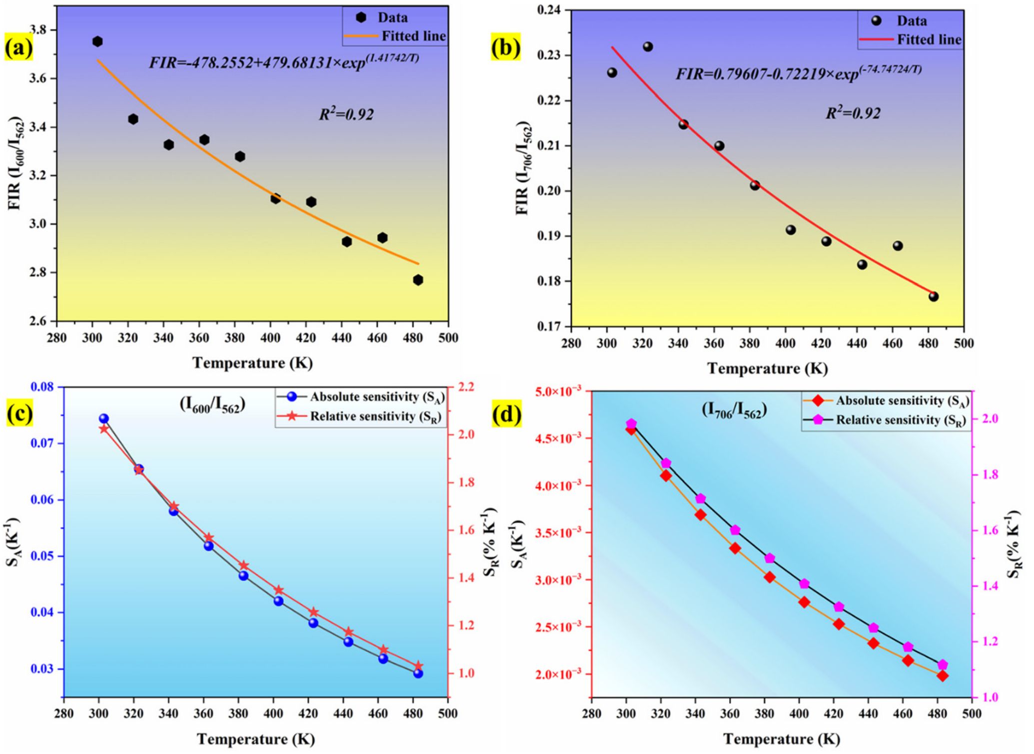

Fig. 19 (a) Fluorescence intensity ratio for I_{600}/I_{562} (b) fluorescence intensity ratio for I_{706}/I_{562} (c) S_A and S_R for I_{600}/I_{562} using Boltzmann distribution (d) S_A and S_R for I_{706}/I_{562}.

temperatures. For (I_{600}/I_{562}), the maximum relative sensitivity was found to be 2.02% K^{-1} at 303 K and S_A as 0.074 K^{-1} at 303 K. Similarly for other transition (I_{706}/I_{562}), the maximum relative sensitivity was found to be 1.98% K^{-1} at 303 K and S_A as 0.0045 K^{-1} at 303 K. Since the intensity counts are less for 706 nm compared to 600 nm the sensitivities also decreased which also revealed that sensitivity is directly in line with intensity of emission. Table 4 lists a few bright thermometers based on Sm^{3+} doped phosphors that have been previously discussed. It is demonstrated that the $Ba_2ZnSi_2O_7:Sm^{3+}$ (x = 0.4 mol%) phosphor has a rather high S_R value. The $Ba_2ZnSi_2O_7:Sm^{3+}$ phosphor may therefore be employed in optical thermometry and show good optical thermometric performance.

Fluorescence lifetime method. We also obtained measurements of the $Ba_2ZnSi_2O_7:Sm^{3+}$ decay curves at 600 nm emission when excited at 403 nm over the temperature range of 303–483 K as shown in Fig. 20(a). The decay curves are found to be well-fitted to the single exponential decay equation given below,[91,92]

$$I(t) = I_0 + \exp\left(-\frac{t}{\tau}\right) \tag{30}$$

where I_0 and $I(t)$ are the luminescence intensities at times 0 and t, respectively, and τ is the decay time. The decay of $Ba_2ZnSi_2O_7:Sm^{3+}$ for different temperatures fits very well in eqn (30). At 303, 323, 343, 363, 383, 403, 423, 443, 463, and 483 K, the decay lifetimes are found to be 1.56, 1.57, 1.58, 1.59, 1.60, 1.61, 1.62, 1.64, 1.66, and 1.69 ms. It is evident from Fig. 20(b) that temperature has a significant impact on the emission decay characteristics of $Ba_2ZnSi_2O_7:Sm^{3+}$. Under stimulation with 403 nm, the lifespan slightly increases from 1.569 ms at 303 K to 1.692 ms at 483 K. Moreover, the thermal-quenching activation energy of Sm^{3+} is found to be 2045.169 cm^{-1}. Using equations given below, which resemble the FIR-based method, can be used to compute the absolute sensitivity $S_{A\text{-lifetime}}$ and the relative sensitivity $S_{R\text{-lifetime}}$ based on the emission lifespan of Sm^{3+}, respectively.[93,94]

$$S_A = \left|\frac{\partial \tau}{\partial T}\right| = (\tau - \tau^2\tau_0)\frac{\Delta E}{k_B T^2} \tag{31}$$

$$S_R = \frac{1}{\tau}\left|\frac{\partial \tau}{\partial T}\right| \times 100 = (1 - \tau\tau_0)\frac{\Delta E}{k_B T^2} \times 100 \tag{32}$$

Based on the Sm^{3+} emission lifetime, Fig. 20(c) displays the absolute sensitivity $S_{A\text{-lifetime}}$ and the relative sensitivity $S_{R\text{-lifetime}}$. The basic trend for both $S_{A\text{-lifetime}}$ and $S_{R\text{-lifetime}}$ is different in this case. Relative sensitivity decreased as we increased the temperature providing a maximum relative sensitivity of 3.25% K^{-1} at 303 K, but absolute sensitivity initially decreased up to 343 K, later reached the maximum of 0.0167 K^{-1} at 363 K and started to decrease up to high temperature. Thus, the highest values of $S_{A\text{-lifetime}}$ and $S_{R\text{-lifetime}}$ are determined to be 0.0167 K^{-1} at 363 K and 3.25% K^{-1} at 303 K respectively. The lifetime-based value of S_R is higher than the FIR-based S_R value when the relative sensitivity values based on lifetime and FIR are compared. This is because the Sm^{3+} emission in the FIR-based system varies very little. Temperature-related changes in emission intensity cause a

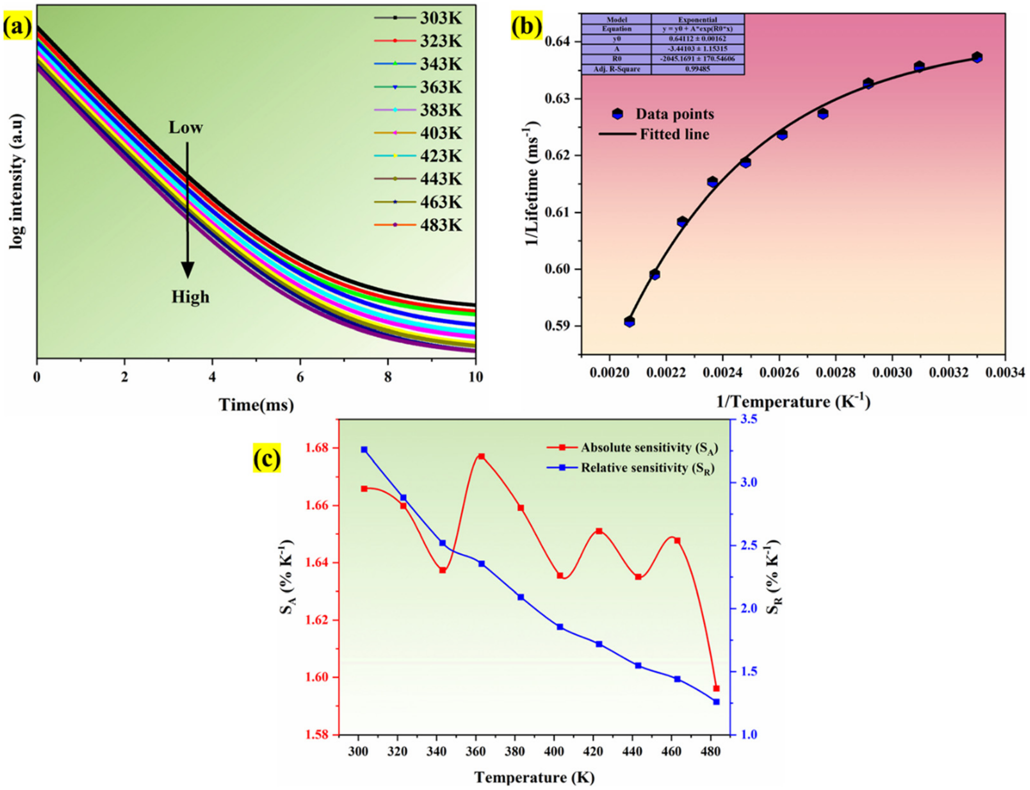

Fig. 20 (a) Temperature-dependent lifetime spectra (b) inverse of lifetime of Sm^{3+} emission *versus* 1/temperature (c) the relative sensitivity S_R and absolute sensitivity S_A based on the emission lifetime of Sm^{3+}.

little shift, but they have minimal effect on the FIR. Table 5 shows that the values of S_R based on both lifetime and FIR are better than prior findings.

Conclusion

$Ba_2ZnSi_2O_7:Sm^{3+}$ phosphors with varying doping concentrations were successfully synthesized using the high-temperature solid-state reaction method. XRD patterns and refinements confirmed the satisfied phase purity and unaltered monoclinic crystal structure with the $C2/c$ space group after Sm^{3+} doping. The phosphor emits orangish-red light at 600 nm under UV excitation, and the optimal Sm^{3+} dopant concentration was determined to be $x = 0.004$ mol. The photoluminescent emission spectra show red and yellow emissions corresponding to the $^4G_{5/2} \rightarrow {}^6H_{5/2}$, $^4G_{5/2} \rightarrow {}^6H_{7/2}$, $^4G_{5/2} \rightarrow {}^6H_{9/2}$, and $^4G_{5/2} \rightarrow {}^6H_{11/2}$ transitions of Sm^{3+}. Concentration quenching was observed due to dipole–dipole interaction, as investigated using the Dexter theory. The optimized phosphor's CIE chromaticity coordinates and CCT value were found to be (0.6017, 0.3976) and 1439 K respectively with 100% color purity. The optical band gap was determined to be 3.40 eV. FTIR spectra confirmed the various Ba–O, Zn–O, and Si–O vibrational modes and the absence of additional phases during phosphor preparation. The phosphor exhibited excellent thermal stability up to 600 °C and a 30% drop in emission intensity compared to ambient temperature at high temperatures. The activation energy and phonon energy were calculated to be 0.359 eV and 63.83 cm^{-1}, respectively. The quenching temperature was found to be 367 K. The $Ba_2ZnSi_2O_7:0.004Sm^{3+}$ phosphor demonstrated excellent temperature sensing performance using the FIR strategy of I_{600}/I_{562}, with a maximum relative sensitivity (S_R) value of 2.02% K^{-1} at 303 K. The fluorescence lifetime of Sm^{3+} luminescence (λ_{Exci} = 403 nm, λ_{Emi} = 600 nm) slowly increased with increasing temperature, suggesting its suitability for lifetime-based luminous thermometry with a maximum S_R value of 3.25% K^{-1} at 303 K. This dual-mode optical temperature sensing approach, based on both FIR and variable lifetime, is a novel design concept presented for the first time in this study.

Table 5 Temperature-sensitive properties based on RE-doped luminescent materials

Materials	Temperature range (K)	$S_{R\text{-max}}$ (% K^{-1})	Mode	Ref.
$Ca_2LaNbO_6:Sm^{3+}$	313–573	0.23	FIR	95
$YVO_4:Sm^{3+}$	299–466	0.31	FIR	96
$YNbO_4:Sm^{3+}$	303–773	0.43	FIR	97
$SrMoO_4:Sm^{3+}$	273–573	0.60	FIR	98
$Ca_3LiMgV_3O_{12}:Sm^{3+}$	303–483	1.600	FIR	99
$Sr_2YF_7:Tm^{3+}$	303–663	1.16	FLT	100
$CaGdMgSbO_6:Mn^{4+}/Sm^{3+}$	298–575	1.23	FLT	91
$BaGd_2O_4:Bi^{3+}/Sm^{3+}$	293–473	1.66	FLT	101
$Sr_2V_2O_7:Sm^{3+}$	38–298	3.12	FLT	102
$Lu_2MoO_6:Sm^{3+}$	273–483	4.9	FLT	103
$Ba_2ZnSi_2O_7:Sm^{3+}$	303–483	2.02	FIR	This work
		3.25	FLT	

The optimized phosphor's good thermal stability, high activation energy, and excellent thermal sensing abilities make it a promising candidate for practical applications in optical temperature detection.

Author contributions

Tejas: methodology, formal analysis, validation, investigation, data curation, writing – original draft, writing – review & editing. Princy A: validation, software, resources, investigation. S Masilla Moses Kennedy: visualization, software, resources. Vikash Mishra – validation, resources, software. M. I. Sayyed – investigation, validation, resources. Taha. A. Hanafy – resources, software. Sudha D. Kamath: writing – review & editing, visualization, validation, supervision, resources, project administration, investigation, formal analysis, data curation.

Data availability

The data that support the findings of this study are available from the corresponding author upon reasonable request.

Conflicts of interest

The authors declare that they have no known competing financial interests or personal relationships that could have appeared to influence the work reported in this paper.

Acknowledgements

The authors acknowledge the financial support from the Manipal Academy of Higher Education to carry out this research work.

References

1 G. B. Nair, H. C. Swart and S. J. Dhoble, A review on the advancements in phosphor-converted light emitting diodes (pc-LEDs): phosphor synthesis, device fabrication and characterization, *Prog. Mater. Sci.*, 2020, **109**, 100622.

2 K. Yang, Y. Shen, K. He, T. Zhang, R. Xu and S. Zhao, *et al.*, An optical fiber temperature sensor based on fluorescence intensity ratio used for real-time monitoring of chemical reactions, *Ceram. Int.*, 2021, **47**(23), 33537–33543.

3 T. Q. Trung, T. M. L. Dang, S. Ramasundaram, P. T. Toi, S. Y. Park and N. E. Lee, A Stretchable Strain-Insensitive Temperature Sensor Based on Free-Standing Elastomeric Composite Fibers for On-Body Monitoring of Skin Temperature, *ACS Appl. Mater. Interfaces*, 2019, **11**(2), 2317–2327.

4 R. Chen, T. Luo, D. Geng, Z. Shen and W. Zhou, Facile fabrication of a fast-response flexible temperature sensor via laser reduced graphene oxide for contactless human-machine interface, *Carbon N. Y.*, 2022, **187**, 35–46.

5 G. Yan, T. Wang, L. Zhu, F. Meng and W. Zhuang, A novel strain-decoupled sensitized FBG temperature sensor and its applications to aircraft thermal management, *Opt. Laser Technol.*, 2021, **140**, 106597.

6 B. Arman Kuzubasoglu and S. Kursun Bahadir, Flexible temperature sensors: a review, *Sens. Actuators, A*, 2020, **315**, 112282.

7 Y. Guo, J. Xie, M. Yu, W. Huang, H. Yang and X. Li, *et al.*, The enhanced up-conversion green by Yb–Mn dimer in $NaBiF_4$:Yb^{3+}/Er^{3+}/Mn^{2+} for optical fiber temperature sensor, *J. Alloys Compd.*, 2021, **888**, 161497.

8 J. Wang, H. Shen, Y. Xia and S. Komarneni, Light-activated room-temperature gas sensors based on metal oxide nanostructures: a review on recent advances, *Ceram. Int.*, 2021, **47**, 7353–7368.

9 D. Chen, M. Xu, S. Liu and X. Li, Eu^{2+}/Eu^{3+} dual-emitting glass ceramic for self-calibrated optical thermometry, *Sens. Actuators, B*, 2017, **246**, 756–760.

10 V. Lojpur, Ž. Antić and M. D. Dramićanin, Temperature sensing from the emission rise times of Eu^{3+} in SrY_2O_4, *Phys. Chem. Chem. Phys.*, 2014, **16**(46), 25636–25641.

11 W. Xu, H. Zhao, Y. Li, L. Zheng, Z. Zhang and W. Cao, Optical temperature sensing through the upconversion luminescence from Ho^{3+}/Yb^{3+} codoped $CaWO_4$, *Sens. Actuators, B*, 2013, **188**, 1096–1100.

12 I. E. Kolesnikov, A. A. Kalinichev, M. A. Kurochkin, E. Y. Kolesnikov and E. Lähderanta, Porphyrins as efficient ratiometric and lifetime-based contactless optical thermometers, *Mater. Des.*, 2019, **184**, 108188.

13 I. E. Kolesnikov, M. A. Kurochkin, E. V. Golyeva, D. V. Mamonova, A. A. Kalinichev and E. Y. Kolesnikov, *et al.*, Multimode high-sensitivity optical YVO_4:Ln^{3+} nanothermometers (Ln^{3+} = Eu^{3+}, Dy^{3+}, Sm^{3+}) using charge transfer band features, *Phys. Chem. Chem. Phys.*, 2020, **22**(48), 28183–28190.

14 S. Lin, Z. Liao, H. Zheng, C. Li, Y. Cui and Z. Wang, *et al.*, A polarized luminescence thermometer based on a dye encapsulated metal–organic framework, *J. Mater. Chem. C*, 2024, **12**(7), 2391–2397.

15 Y. Patle, N. Brahme, D. P. Bisen, T. Richhariya, E. Chandrawanshi and A. Choubey, *et al.*, Study of Photoluminescence,Thermoluminescence, and Afterglow properties of Dy^{3+} doped $Ba_2ZnSi_2O_7$ phosphor, *Optik*, 2021, **226**, 165896.

16 I. Gupta, S. Singh, S. Bhagwan and D. Singh, Rare earth (RE) doped phosphors and their emerging applications: a review, *Ceram. Int.*, 2021, **47**, 19282–19303.

17 H. R. Shih and Y. S. Chang, Structure and photoluminescence properties of Sm^{3+} ion-doped $YInGe_2O_7$ phosphor, *Materials*, 2017, **10**(7), 779.

18 A. Z. M. Al-Juboori, Rare earth (Sm^{3+} and Dy^{3+})-doped gadolinium oxide nanomaterials for luminescence thermometry, *Phys. Scr.*, 2013, 014004.

19 S. Sharma, S. Kumar Dubey and A. K. Diwakar, Luminescence investigation on $Ca_2MgSi_2O_7$:Eu^{2+},Dy^{3+} phosphor, *Int. J. Mater. Sci.*, 2021, **2**(2), 08–15.

20 K. Igashira, D. Nakauchi, T. Ogawa, T. Kato, N. Kawaguchi and T. Yanagida, Effects of dopant concentration in

Eu-doped $Ca_2MgSi_2O_7$ single crystalline scintillators, *Mater. Res. Bull.*, 2021, **135**, 111155.

21 S. Sharma and S. K. Dubey, 5 Structural, morphological, thermal, and long persistent properties of synthesized nanostructured phosphor, *Nanocomposite Nanohybrid Mater.: Process. Appl.*, 2023, **17**, 99.

22 I. P. Sahu, D. P. Bisen and N. Brahme, Luminescence properties of green-emitting $Ca_2MgSi_2O_7$:Eu^{2+} phosphor by a solid-state reaction method, *Luminescence.*, 2015, **30**(7), 1125–1132.

23 Y. Wang, S. Wu, W. Lei, M. Wu, Y. Wang and F. Li, *et al.*, A new method for preparing cubic-shaped $Sr_2MgSi_2O_7$:Eu^{2+},Dy^{3+} phosphors and the effect of sintering temperature, *Ceram. Int.*, 2022, **48**(4), 5397–5403.

24 M. A. Tshabalala, H. C. Swart, F. B. Dejene, E. Coetsee and O. M. Ntwaeaborwa, Structure, surface analysis, photoluminescent properties and decay characteristics of Tb^{3+}–Eu^{3+} co-activated $Sr_2MgSi_2O_7$ phosphor, *Appl. Surf. Sci.*, 2016, **360**, 409–418.

25 W. Teng, H. Dong, C. Hu, X. Yang, J. Wang and X. Liang, *et al.*, Achieving multi-wavelength excitation and multicolor tunable emission in self-reducing phosphor of $Ba_2MgSi_2O_7$:Eu^{2+}/Eu^{3+}, *J. Lumin.*, 2024, **269**, 120524.

26 R. Cao, J. Wei, T. Chen, B. Lan, L. Li and R. Liu, *et al.*, Synthesis, adjustable-color emission and energy transfer of $Ba_2MgSi_2O_7$:Sm^{3+},Bi^{3+} phosphors, *J. Mol. Struct.*, 2023, **1274**, 134404.

27 X. Shui, C. Zou, W. Zhang, C. Bao and Y. Huang, Effect of M^{3+} (M = Bi, Al) co-doping on the luminescence enhancement of $Ca_2ZnSi_2O_7$:Sm^{3+} orange-red-emitting phosphors, *Ceram. Int.*, 2021, **47**(6), 8228–8235.

28 C. Yao and C. Zhang, Photoluminescence enhancement and excellent thermal stability of $Ca_2ZnSi_2O_7$:Pr^{3+} red-emitting phosphors through charge compensator A^+ (Li^+, Na^+ and K^+) co-doping for w-LED applications, *Spectrochim. Acta, Part A*, 2023, **303**, 123177.

29 S. Chandraker, J. Kaur, R. Priya, V. Dubey and N. Dubey, White light emission and thermoluminescence studies of Dy^{3+}-activated hardystonite ($Ca_2ZnSi_2O_7$) phosphor, *Luminescence*, 2021, **36**(6), 1507–1512.

30 B. Tian, K. Chen, J. Zhou, F. Shang, A. Manan and G. Chen, Photoluminescence properties of Eu^{3+} and Al^{3+}-doped $Ca_2ZnSi_2O_7$ red phosphors for plant growth LEDs, *J. Mater. Sci.: Mater. Electron.*, 2024, **35**(12), 863.

31 V. Singh, N. Deopa, S. Kaur, A. S. Rao, J. L. Rao and G. Lakshminarayana, EPR and Optical Properties of Green Emitting Mn Activated $Sr_2ZnSi_2O_7$ Phosphors Prepared by Sol–Gel Method, *J. Electron. Mater.*, 2020, **49**(3), 2265–2272.

32 S. Chandraker, J. Kaur, V. Dubey and N. Dubey, Composite nature of thermo luminescence studies in Dy^{3+} activated $Sr_2ZnSi_2O_7$ phosphor, *Optik*, 2021, **241**, 166904.

33 S. Chandraker, J. Kaur and V. Dubey, Determination of spectroscopic parameters and thermoluminescence studies of Dy^{3+}-activated $Ba_2ZnSi_2O_7$ phosphor, *Radiat. Eff. Defects Solids*, 2021, **176**(11–12), 1116–1128.

34 Z. Yang, Y. Hu, L. Chen and X. Wang, Color tuning of $Ba_2ZnSi_2O_7$:Ce^{3+},Tb^{3+} phosphor via energy transfer, *J. Lumin.*, 2014, **153**, 412–416.

35 S. Deng, Z. Qiu, M. Zhang, W. Zhou, J. Zhang and C. Li, *et al.*, Tricolor emitting and energy transfer in the phosphor $Ba_2ZnSi_2O_7$:Ce^{3+},Eu^{3+},Eu^{2+} for white-LED based near-UV chips, *J. Rare Earths*, 2015, **33**(5), 463–468.

36 Z. Y. Zou, K. Du, X. K. Lan, W. Z. Lu, X. C. Wang and X. H. Wang, *et al.*, Anti-reductive characteristics and dielectric loss mechanisms of $Ba_2ZnSi_2O_7$ microwave dielectric ceramic, *Ceram. Int.*, 2019, **45**(15), 19415–19419.

37 A. M. Pire and M. R. Davolos, Luminescence of europium(III) and manganese(II) in barium and zinc orthosilicate, *Chem. Mater.*, 2001, **13**(1), 21–27.

38 H. Li, R. Pang, G. Liu, W. Sun, D. Li and L. Jiang, *et al.*, Synthesis and Luminescence Properties of Bi^{3+}-Activated K_2MgGeO_4: A Promising High-Brightness Orange-Emitting Phosphor for WLEDs Conversion, *Inorg. Chem.*, 2018, **57**(19), 12303–12311.

39 R. Naik, S. C. Prashantha, H. Nagabhushana, H. P. Nagaswarupa, K. S. Anantharaju and S. C. Sharma, *et al.*, Mg_2SiO_4:Tb^{3+} nanophosphor: auto ignition route and near UV excited photoluminescence properties for WLEDs, *J. Alloys Compd.*, 2014, **617**, 69–75.

40 R. Hepzi and P. Devamani, Synthesis and characterization of barium hydroxide nanoparticles, *Asian Acad. Res. J. Multidisciplinary*, 2014, 58–68.

41 M. Riaz, H. Imtiaz, M. Hussain, A. Qamar, F. Bashir and T. Hussain, A study on synthesis and characterization of non-stoichiometric hardystonite $Ca_2ZnSi_2O_7$ for optical and dielectric applications, *Opt. Mater.*, 2022, **131**, 112699.

42 C. Kumas and A. Obut, Effect of heating on structure and leaching characteristics of a zinc carbonate ore, *Physicochem. Probl. Miner. Process.*, 2021, **57**(5), 23–32.

43 X. Zhang, C. Zhang, Y. Li, J. Li, J. Zhang, H. Liu, W. Ai, R. Wang, D. Huang and C. K. Mahadevan, Structural and optical properties of Sm^{3+} doped Sr_2SiO_4 phosphor prepared from coal gasification slag for the LED application, *Opt. Mater.*, 2024, **148**, 114954.

44 A. S. Priya, S. Ramachandran, S. D. Vasantha and H. P. Kumar, Delineating Dy^{3+} and Sm^{3+} in thermally stable strontium silicate apatites for multifunctional applications, *J. Mol. Struct.*, 2024, **1312**, 138540.

45 Y. Li, S. Xu, J. Chen, Y. Gao, X. Zhang, K. Pang, H. Liu, Y. Chi, X. Sun and C. K. Mahadevan, A novel Sm^{3+} doped niobium silicate luminescent glass with high thermal stability for the temperature sensing and LED applications, *Opt. Mater.*, 2024, **153**, 115607.

46 G. Ramakrishna, H. Nagabhushana, S. C. Prashantha, S. C. Sharma and B. M. Nagabhushana, Role of flux on morphology and luminescence properties of Sm^{3+} doped Y_2SiO_5 nanopowders for WLEDs, *Spectrochim. Acta, Part A*, 2015, **136**(PB), 356–365.

47 G. S. R. Raju and S. Buddhudu, Emission analysis of Sm^{3+} and Dy^{3+}:$MgLaLiSi_2O_7$ powder phosphors, *Spectrochim. Acta, Part A*, 2008, **70**(3), 601–605.

48 B. V. Ratnam, M. Jayasimhadri and K. Jang, Luminescent properties of orange emissive Sm^{3+}-activated thermally stable phosphate phosphor for optical devices, *Spectrochim. Acta, Part A*, 2014, **132**, 563–567.

49 Z. Wang, P. Li, Z. Yang and Q. Guo, A novel red phosphor $BaZn_2(PO_4)_2:Sm^{3+},R^+$ (R = Li, Na, K), *J. Lumin.*, 2012, **132**(8), 1944–1948.

50 R. Yu, H. Mi Noh, B. Kee Moon, B. Chun Choi, J. Hyun Jeong and H. Sueb Lee, *et al.*, Photoluminescence characteristics of Sm^{3+}-doped Ba_2CaWO_6 as new orange-red emitting phosphors, *J. Lumin.*, 2014, **152**, 133–137.

51 Z. Wu, B. Chen, X. Li, J. Zhang, J. Sun and H. Zhong, *et al.*, Optical transition properties, energy transfer mechanism and luminescent thermal stability of Sm^{3+}-doped silicate glasses, *J. Alloys Compd.*, 2016, **663**, 545–551.

52 S. A. R. Sekaran, R. K. Padhi, E. S. Yousef and K. Marimuthu, Spectroscopic studies on Sm^{3+} ions doped modifiers incited calcium phospho-silicate glasses for photonic and optoelectronic applications, *J. Non-Cryst. Solids*, 2024, **623**, 122692.

53 Q. Xu, J. Sun, D. Cui, Q. Di and J. Zeng, Synthesis and luminescence properties of novel $Sr_3Gd(PO_4)_3:Dy^{3+}$ phosphor, *J. Lumin.*, 2015, **158**, 301–305.

54 X. Wu, X. Zhao, Q. Ren, L. Du, M. Pei and O. Hai, Design efficient energy transfer $Ca_2Al_2SiO_7:Bi^{3+},Eu^{3+}$ phosphors by cationic substitution for full-spectrum W-LED lighting, *Ceram. Int.*, 2023, **49**(11), 18852–18860.

55 D. L. Dexter, A theory of sensitized luminescence in solids, *J. Chem. Phys.*, 1953, **21**(5), 836–850.

56 K. Cheng, Y. Xu, X. Liu, J. Long, W. Huang and C. Deng, A novel far-red phosphors $Li_2ZnTi_3O_8:Cr^{3+}$ for indoor plant cultivation: synthesis and luminescence properties, *Ceram. Int.*, 2023, **49**(4), 6343–6350.

57 T. M. Mazzo, M. L. Moreira, I. M. Pinatti, F. C. Picon, E. R. Leite and I. L. V. Rosa, *et al.*, $CaTiO_3:Eu^{3+}$ obtained by microwave assisted hydrothermal method: a photoluminescent approach, *Opt. Mater.*, 2010, **32**(9), 990–997.

58 in *Luminescence of Inorganic Solids*, ed. B. Di Bartolo, V. Godberg and D. Pacheco, Springer US, Boston, MA, 1978. Available from: **https://link.springer.com/10.1007/978-1-4684-3375-3**.

59 A. K. Vishwakarma, K. Jha, M. Jayasimhadri, B. Sivaiah, B. Gahtori and D. Haranath, Emerging cool white light emission from Dy^{3+} doped single phase alkaline earth niobate phosphors for indoor lighting applications, *Dalton Trans.*, 2015, **44**(39), 17166–17174.

60 C. S. McCamy, Correlated color temperature as an explicit function of chromaticity coordinates, *Color Res. Appl.*, 1992, **17**(2), 142–144.

61 P. Sharma and M. Jayasimhadri, Exploration of efficient photoluminescence properties of intense green emitting Er^{3+} activated $NaBi(MoO_4)_2$ phosphor for white LED applications, *J. Mater. Res.*, 2023, **38**(20), 4655–4664.

62 S. G. M. Mushtaque, A. R. Kadam and S. J. Dhoble, High color purity and color tunability in Sm^{3+}/Eu^{3+} activated/co-activated $Sr_6Ca_4(PO_4)_6F_2$ phosphor for WLED and display devices application, *J. Mol. Struct.*, 2023, **1274**, 134510.

63 R. M. Evans and B. K. Swenholt, Chromatic Strength of Colors: Dominant Wavelength and Purity, *J. Opt. Soc. Am.*, 1967, **57**(11), 1319–1324.

64 Y. C. Jiang, Y. Tong, S. Y. Z. Chen, W. N. Zhang, F. F. Hu and R. F. Wei, *et al.*, A three-mode self-referenced optical thermometry based on up-conversion luminescence of $Ca_2MgWO_6:Er^{3+},Yb^{3+}$ phosphors, *Chem. Eng. J.*, 2021, **413**, 127470.

65 R. Mahajan and R. Prakash, Effect of Sm^{3+} doping on optical properties of $Mg_2P_2O_7$ and $Mg_3P_2O_8$ phosphors, *Mater. Chem. Phys.*, 2020, **246**, 122826.

66 M. Farooq, M. H. Rasool, H. Rafiq, I. Nazir and S. Rubab, Synthesis, characterization and optical tuning of Sm^{3+} doped $NaZnPO_4$ phosphors for white LED technology, *Ceram. Int.*, 2024, **50**(12), 21118–21129.

67 P. Khajuria, V. D. Sharma, A. Khajuria, R. Prakash and R. J. Choudhary, Synthesis and Spectroscopic Investigations of Sm^{3+} Activated ZrO_2 and Na_2ZrO_3 as Warm Light Phosphors, *J. Fluoresc.*, 2024, 1–16.

68 A. Saeed, S. Sobaih, W. A. Abu-raia, A. Abdelghany and S. Heikal, Novel Er^{3+} doped heavy metals-oxyfluorophosphate glass as a blue emitter, *Opt. Quantum Electron.*, 2021, **53**(8), 482.

69 G. Sun and Q. Chen, Novel red-emitting $Ca_2LiScB_4O_{10}:Sm^{3+}$ phosphor for WLED: photoluminescence, thermal stability, crystal structure, Judd-Ofelt parameters and energy band gap studies, *J. Alloys Compd.*, 2023, **936**, 168263.

70 L. S. Archana, D. N. Rajendran, K. Sreelatha and J. Cyriac, Effect of Sm^{3+} ions doping on the structural and optical properties, Judd-Ofelt and radiative parameters of ZnS phosphor materials, *Mater. Chem. Phys.*, 2023, **305**, 127934.

71 R. Cao, T. Huang, J. Nie, L. Zhang, Y. Chen and L. Li, *et al.*, Energy transfer and tunable-color luminescence properties of a single-phase $CaSrNb_2O_7:Sm^{3+},Bi^{3+}$, *J. Mol. Struct.*, 2024, **1297**, 136962.

72 C. Y. Chang, T. H. Hsu and C. L. Huang, Novel and thermostable double-perovskite $La_2ZnTiO_6:Sm^{3+},Dy^{3+}$ phosphors with high quantum efficiency, *Opt. Mater.*, 2023, **135**, 113361.

73 R. Cao, J. Lin, B. Lan, F. Cheng, T. Chen and L. Li, *et al.*, Luminescence properties, tunable emission and energy transfer of $Na_3Sc_2(PO_4)_3:Sm^{3+},Bi^{3+}$ phosphors, *J. Mol. Struct.*, 2023, **1282**, 135221.

74 X. Li, J. Ding, Z. Tang, X. Lin, H. Dong and A. Wu, *et al.*, Novel orange-red emitting $Sr_3Ga_2Ge_4O_{14}:Sm^{3+}$ phosphors with high color purity for red-backlight display and white LEDs, *Ceram. Int.*, 2024, **50**, 20–28.

75 A. Y. Madkhli, H. Kaynar, M. B. Coban, M. Ayvacikli, A. Canimoglu and N. Can, Characterization, room and low temperature photoluminescence of yttrium aluminium borate activated with Sm^{3+} ions, *Mater. Res. Bull.*, 2023, **161**, 112167.

76 L. Mukhopadhyay and V. K. Rai, Thermally stable red emitting xenotime phosphate nanophosphors for displays, *Mater. Res. Bull.*, 2020, **121**, 110628.

77 M. Prasad and V. K. Rai, Coactivated cyan emitting phosphors in optical thermometry using thermally and non-thermally coupled levels, *Mater. Res. Bull.*, 2023, **160**, 112116.

78 S. Pattnaik and V. K. Rai, Tailoring of upconversion luminescence of Al^{3+} engineered titanate phosphor for non-invasive thermometry, *Methods Appl. Fluoresc.*, 2022, **10**(3), 034002.

79 Y. Yang, Z. Lu, H. Fan, M. Chen, L. Shen and X. Zhang, *et al.*, Ultra-Broadband Near-Infrared Phosphors Realized by the Heterovalent Substitution Strategy, *Inorg. Chem.*, 2023, **62**(8), 3601–3608.

80 D. Wu, L. Liu, H. Liang, H. Duan, W. Nie and J. Wang, *et al.*, $LiBAlF_6:Cr^{3+}$ (B = Ca, Sr) fluoride phosphors with ultra-broad near-infrared emission for NIR pc-LEDs, *Ceram. Int.*, 2022, **48**(1), 387–396.

81 Z. Tian, B. Liu, Y. Xiao, Z. Wang, L. Zhang and S. Xu, *et al.*, Unveiling the phonon effect on the narrow-band deep-red emission from solution–combustion synthesized Mn^{4+} doped $CaYAlO_4$ microcrystals, *J. Alloys Compd.*, 2022, **923**, 166280.

82 C. Li, F. Tang, Y. Xiao, Y. Zhou, B. Zhao and S. Lv, High brightness and vibronic luminescent behavior of YAG: Mn^{4+}/Ca^{2+} red phosphor for preparing phosphor-in-glass in white LED, *J. Mater. Chem. C*, 2023, **11**(41), 14413–14420.

83 J. W. de Wit, T. P. van Swieten, M. A. van de Haar, A. Meijerink and F. T. Rabouw, Increasing the Power: Absorption Bleach, Thermal Quenching, and Auger Quenching of the Red-Emitting Phosphor $K_2TiF_6:Mn^{4+}$, *Adv. Opt. Mater.*, 2023, **11**(9), 2202974.

84 B. Vasanthi, N. Gopakumar and P. S. Anjana, Thermally stable and red emitting bismuth ions sensitized $SrGa_2O_4:Eu^{3+}$ phosphors for phosphor converted WLED applications, *Solid State Sci.*, 2024, **151**, 107526.

85 J. Zheng, Q. Cheng, C. Zheng, G. Chen, F. Shi and C. Chen, Correlated color temperature tunability and energy transfer phenomenon in the $NaBaBO_3:Dy^{3+}/Eu^{3+}$ phosphor for white light application. Functional, *Mater. Lett.*, 2015, **8**(6), 1550077.

86 B. Klimesz, R. Lisiecki and W. Ryba-Romanowski, Sm^{3+}-doped oxyfluorotellurite glasses – spectroscopic, luminescence and temperature sensor properties, *J. Alloys Compd.*, 2019, **788**, 658–665.

87 J. Liao, M. Wang, L. Kong, J. Chen, X. Wang, H. Yan, J. Huang and C. Tu, Dual-mode optical temperature sensing behavior of double-perovskite $CaGdMgSbO_6$: Mn^{4+}/Sm^{3+} phosphors, *J. Lumin.*, 2020, **226**, 117492.

88 Q. Chen, X. Yang, G. Zhang, Q. Ma, S. Han and B. Ma, Color-tunable Eu^{3+} – or Sm^{3+}-doped perovskite phosphors as optical temperature-sensing materials, *Opt. Mater.*, 2021, **111**, 110585.

89 Y. Gao, F. Huang, H. Lin, J. Zhou, J. Xu and Y. Wang, A Novel Optical Thermometry Strategy Based on Diverse Thermal Response from Two Intervalence Charge Transfer States, *Adv. Funct. Mater.*, 2016, **26**(18), 3139–3145.

90 F. Huang and D. Chen, Synthesis of $Mn^{2+}:Zn_2SiO_4$-$Eu^{3+}:Gd_2O_3$ nanocomposites for highly sensitive optical thermometry through the synergistic luminescence from lanthanide-transition metal ions, *J. Mater. Chem. C*, 2017, **5**(21), 5176–5182.

91 J. Liao, M. Wang, L. Kong, J. Chen, X. Wang and H. Yan, *et al.*, Dual-mode optical temperature sensing behavior of double-perovskite $CaGdMgSbO_6:Mn^{4+}/Sm^{3+}$ phosphors, *J. Lumin.*, 2020, **226**, 117492.

92 S. Zhang and Y. Hu, Photoluminescence spectroscopies and temperature-dependent luminescence of Mn^{4+} in $BaGe_4O_9$ phosphor, *J. Lumin.*, 2016, **177**, 394–401.

93 A. Mamedov, Urbach rule and optical properties of the $LiNbO_3$ and $LiTaO_3$, *J. Opt. A: Pure Appl. Opt.*, 1999, **1**(3), 424.

94 H. Luo, X. Li, X. Wang and M. Peng, Highly thermal-sensitive robust $LaTiSbO_6:Mn^{4+}$ with a single-band emission and its topological architecture for single/dual-mode optical thermometry, *Chem. Eng. J.*, 2020, **384**, 1223272.

95 A. Zhang, Z. Sun, M. Jia, Z. Fu, B. C. Choi and J. H. Jeong, *et al.*, Sm^{3+}-doped niobate orange-red phosphors with a double-perovskite structure for plant cultivation and temperature sensing, *J. Alloys Compd.*, 2022, **889**, 161671.

96 I. E. Kolesnikov, E. V. Golyeva, M. A. Kurochkin, E. Y. Kolesnikov and E. Lähderanta, Concentration series of Sm^{3+}-doped YVO_4 nanoparticles: structural, luminescence and thermal properties, *J. Lumin.*, 2020, **219**, 116946.

97 L. R. Dačanin, S. R. Lukić-Petrović, D. M. Petrović, M. G. Nikolić and M. D. Dramićanin, Temperature quenching of luminescence emission in Eu^{3+} – and Sm^{3+}-doped $YNbO_4$ powders, *J. Lumin.*, 2014, **151**, 82–87.

98 X. Tian, L. Guo, J. Wen, L. Zhu, C. Ji and Z. Huang, *et al.*, Anti-thermal quenching behavior of Sm^{3+} doped $SrMoO_4$ phosphor for new application in temperature sensing, *J. Alloys Compd.*, 2023, **959**, 170574.

99 J. Q. Chen, J. Y. Chen, W. N. Zhang, S. J. Xu, L. P. Chen and H. Guo, Three-mode optical thermometer based on $Ca_3LiMgV_3O_{12}:Sm^{3+}$ phosphors, *Ceram. Int.*, 2023, **49**(10), 16252–16259.

100 W. P. Chen, F. F. Hu, R. F. Wei, Q. G. Zeng, L. P. Chen and H. Guo, Optical thermometry based on up-conversion luminescence of Tm^{3+} doped transparent Sr_2YF_7 glass ceramics, *J. Lumin.*, 2017, **192**, 303–309.

101 J. Fu, L. Zhou, Y. Chen, J. Lin, R. Ye and D. Deng, *et al.*, Dual-mode optical thermometry based on Bi^{3+}/Sm^{3+} co-activated $BaGd_2O_4$ phosphor with tunable sensitivity, *J. Alloys Compd.*, 2022, **897**, 163034.

102 H. Li, L. Li, L. Mei, W. Zhao, X. Zhou and Y. Hua, Energy transfer from VO_4^{3-} to Sm^{3+} ions in α-$Sr_2V_2O_7$ phosphors for full-spectrum warm-WLED device and low-temperature luminescence lifetime thermometry, *Mater. Today Chem.*, 2023, **32**, 101661.

103 L. Li, S. Fu, Y. Zheng, C. Li, P. Chen and G. Xiang, *et al.*, Near-ultraviolet and blue light excited Sm^{3+} doped Lu_2MoO_6 phosphor for potential solid-state lighting and temperature sensing, *J. Alloys Compd.*, 2018, **738**, 473–483.